



In-situ probing polarization-induced stability of single-atom alloy electrocatalysts in metal-air battery via synchrotron-based X-ray diffraction

Chandran Balamurugan^{a,b}, Young Yong Kim^c, Yong-Ryun Jo^d, Kyusang Cho^e,
Byoungwook Park^f, Woochul Kim^g, Namsoo Lim^g, Yusin Pak^g, Hyeonghun Kim^h,
Hyeonryul Leeⁱ, Keun Hwa Chae^j, Ji Hoon Shim^{k,l}, Changhoon Lee^{m,*}, Sooncheol Kwon^{a,*}

^a Department of Energy and Materials Engineering, Dongguk University-Seoul, Seoul 04620, Republic of Korea

^b Heeger Center for Advanced Materials (HCAM), Gwangju Institute of Science and Technology (GIST), 123 Cheomdangwagi-ro, Buk-gu, Gwangju 61005, Republic of Korea

^c Pohang Accelerator Laboratory, Pohang University of Science and Technology, Pohang 37673, Republic of Korea

^d GIST Advanced Institute of Instrumental Analysis (GAIA), Electron Microscopy Laboratory, Gwangju Institute of Science and Technology, Gwangju 61005, Republic of Korea

^e Research Institute for Solar and Sustainable Energies (RISE), GIST, 123 Cheomdangwagi-ro, Buk-gu, Gwangju 61005, Republic of Korea

^f Division of Advanced Materials, Korea Research Institute of Chemical Technology (KRICT), Daejeon 34114, Republic of Korea

^g Sensor System Research Center, Korea Institute of Science and Technology (KIST), Seoul 02792, Republic of Korea

^h Ceramic Total Solution Center, Korea Institute of Ceramic Engineering and Technology, Icheon, Gyeonggi 17303, Republic of Korea

ⁱ Department of Advanced battery Convergence Engineering, Dongguk University-Seoul, Seoul, 04620 Republic of Korea

^j Advanced Analysis and Data Center, KIST, Seoul 02792, Republic of Korea

^k Division of Advanced Materials Science, Pohang University of Science and Technology, Pohang, 37673, Republic of Korea

^l Department of Chemistry, Pohang University of Science and Technology, Pohang, 37673, Republic of Korea

^m Max Planck POSTECH Center for Complex Phase of Materials, Pohang University of Science and Technology, Pohang 37673, Republic of Korea

ARTICLE INFO

Keywords:

Single-atom alloy electrocatalysts

ORR/OER and HER

In-situ Raman spectra

Flexible metal-air battery

In-situ synchrotron-based analysis

Reversible electrochemical reaction

ABSTRACT

In this work, a novel single-atom alloy electrocatalyst (SAAE) was developed for enhanced electrocatalysis in next-generation energy technologies. The catalyst, composed of single-atom Rh and bulk Ni on FeV₃O₈ support, overcomes challenges related to stability and efficiency in electrochemical reactions. The work function difference between Rh and Ni, as confirmed by computational and synchrotron-based analysis, facilitates superior electric polarization and ohmic contact with FeV₃O₈. The FeV₃O₈@RhNi demonstrates outstanding performance in oxygen reduction reactions (ORRs) and oxygen evolution reactions (OERs), with high half-wave potential (0.90 V) and low overpotential (120 mV at 10 mA cm⁻²). In zinc-air batteries, it maintains a stable discharge-charge voltage gap, specific capacity of 810 mAh g⁻¹, peak power density of 186 mW cm⁻² at 320 mA cm⁻², and cycle stabilities exceeding 859 h at 10 mA cm⁻². The catalyst also proves its durability in flexible zinc-air batteries, indicating its potential for efficient electrocatalytic reactions in emerging energy technologies.

1. Introduction

Electrochemical catalysts play a crucial role in enabling efficient and cost-effective chemical reactions in a broad range of energy conversion/storage and mobility applications, including fuel cells, electrolyzers, and batteries [1–4]. These catalysts comprise oxidizing and/or reducing agents that can alter the potential at which oxidation and/or reduction processes occur, thus accelerating chemical reactions without being consumed during the process. However, current commercialized

catalysts for these reactions heavily rely on rare and precious metals, such as platinum (Pt), iridium (Ir), and ruthenium (Ru), which are costly and scarce [5]. This dependence severely limits the practical application of electrochemical devices [6]. Therefore, there has been a longstanding desire to develop highly efficient and cost-effective electrocatalysts to advance research in this prosperous field [7–9].

As an alternative to conventional electrocatalysts, single-atom alloy electrocatalysts (SAAEs) are emerging as highly promising catalysts [10–16]. SAAEs comprise isolated metal atoms dispersed on less active

* Corresponding authors.

E-mail addresses: chlee0887@postech.ac.kr (C. Lee), kwansc12@dongguk.edu (S. Kwon).

<https://doi.org/10.1016/j.apcatb.2024.124072>

Received 14 January 2024; Received in revised form 25 March 2024; Accepted 12 April 2024

Available online 16 April 2024

0926-3373/© 2024 The Authors. Published by Elsevier B.V. This is an open access article under the CC BY-NC license (<http://creativecommons.org/licenses/by-nc/4.0/>).

materials such as carbon and metal oxides, which can alter their structural and electronic properties to create uniform and well-defined active sites, thereby maximizing the catalytic activity at a reduced cost [17–20]. In addition, SAAEs can offer tunable coordination environments, enabling exclusive selectivity for specific reactions [21–25]. Despite demonstrating superior activity in various electrochemical reactions, SAAEs have still suffered from limited stability under harsh reaction conditions, challenges in synthesis and characterization, potential issues related to scalability and cost-effectiveness [26–29]. For example, the conventional synthesis of SAAEs typically requires high-cost equipment and high vacuum conditions, resulting in low metal loading (<0.1 wt%) because of the high surface energy of isolated atoms, limiting large-scale production (e.g., mass-selected soft loading and atomic layer loading) [30,31]. Furthermore, the catalytic efficiency of SAAEs is hampered by the low density of single-atom active sites and poor charge transport properties, leading to rapid activity loss under long-term operating conditions.

To overcome the challenges associated with such low stability and catalytic efficiency of SAAEs, many efforts have been devoted to developing 1) novel catalyst support structure or protective coating technology, and 2) tailoring the composition and structure of single-atom, which can improve their electrical property as well as a polarization effect on their surface. In addition, the surface polarization in SAAE might increase an adsorption energy, and thereby improve their structural stability [32]. The degree of polarization in SAAEs is also proportional to their work function (or electronegativity) difference, indicating that the high polarization facilitates the charge transfer process at a heteroatom interface by the incorporation of electron-donating and accepting element precursors [33–35]. Furthermore, the increase of dielectric constant in SAAE could result in a decrease in the electrostatic force between the defects and carriers, which reduced their defect-capture radius [36].

The surface polarization effect of SAAEs on top of a transition metal oxide support would be highly beneficial for secondary battery application (i.e., Zn-air battery) because the nanostructured transition metal oxide (e.g., vanadium oxide) can offer an increased interfacial area and numerous heteroatom interfaces for an efficient charge redistribution and reversible metal/metal oxide transformation. However, designing and synthesizing SAAEs on top of the metal oxide support to promote enhanced electric polarization have been challenging due to weak interatomic interactions during synthesis, resulting in severe aggregation and reduced reproducibility [17,37,38]. Furthermore, to probe the polarization effect of SAAEs on their electrochemical performance and stability, it is necessary to develop a noble *in-situ* observation technology (i.e., Synchrotron-Based X-ray Diffraction) which can track down a dendrite formation or the change of their crystal structure during a full discharge/charge cycle of a battery. Therefore, addressing these issues should involve a consideration of appropriate synthesis methodology for SAAEs with an enhanced electric polarization, as well as an evaluation of *in-situ* electrochemical reaction for metal anode in a full cell of battery.

Recently, several Zn-air battery system have been studied with the aim of understanding their electrocatalytic performance and lifetime behavior using *in-situ* X-ray experiments [39–41]. In 2017, Arlt and colleagues developed a Zn-air battery suitable for X-ray computed tomography [42]. They studied how electrolyte redistribution during discharge affected battery performance and found that pore flooding in the air electrode led to the battery's end of life. Franke-Lang's group later improved the battery design by adjusting the density of the Zn matrix in the anode to reduce stress caused by structural expansion and highlighted how parasitic reactions could deteriorate the anode [43]. Nakata et al. examined artificially grown zinc dendrites and discovered that they could be dissolved using low oxidation currents, impacting battery cycle life [44]. They also used *in situ* X-ray diffraction to study changes in the Zn electrode of a Zn/NiOOH battery and found that preventing non-uniform Zn deposition could improve battery cycle life. Despite the significant efforts on the development of *in-situ* X-ray

measurement for metal-air battery configuration and system above, there has been few *in-situ* studies for the polarization-induced SAAEs on their electrocatalytic efficiency and stability.

In metal-air battery, rhodium (Rh), a 4d transition metal, has been considered as a promising catalyst for a range of critical reactions, including the oxygen reduction reaction (ORR), oxygen evolution reaction (OER), hydrogen evolution reaction (HER), and alcohol oxidation (AOR), due to its unique electronic structures, remarkable properties, and stable chemical characteristics [45–48]. However, the widespread application of Rh materials in catalysis is hindered by their limited availability and high cost. Therefore, there is a significant demand to minimize the usage of Rh while maximizing its intrinsic activity. Alloying Rh with low-cost and abundant 3d transition metals, such as nickel (Ni), copper (Cu), cobalt (Co), and iron (Fe), not only reduces the reliance on precious Rh but also alters its electrocatalytic performance and stability, particularly its intrinsic oxidation and reduction properties. Moreover, the synergistic effects of combining 3d transition metals with Rh can effectively lower the energy barrier of the rate-determining step and increase the number of active sites [49–53]. Thus, the rational synthesis of Rh-transition metal combinations with large surface-to-volume ratios and abundant isolated atoms emerges as a promising strategy to enhance their catalytic performance.

Furthermore, the coupling of single-atom alloys with two-dimensional (2D) transition metal nanomaterials, such as nanoplates and nanosheets, to form heterojunctions represents a compelling approach for advancing energy storage devices [54–57]. Compared to bulk materials, 2D hierarchical nanomaterials exhibit distinct physical, chemical, and structural characteristics, including large specific surface areas, increased exposed interfaces, and anisotropic structures, allowing them promising candidates for metal-air battery applications [58,59]. In a single-atom alloy and 2D nanomaterial heterojunction, the interface preserves the high redox ability of each component while facilitating the separation of charge carriers and enhancing electron and mass transfer rates [60,61]. Consequently, the interface structure of heterogeneous catalysts has garnered significant attention as potential electrocatalyst candidates for fuel cells and metal-air rechargeable batteries [62–66].

Herein, we demonstrate a novel strategy for tuning the electric polarization of SAAEs by deploying single-atom Rh on the bulk Ni surface via a hydrothermal process (referred to here as RhNi). The difference between the work functions (Φ) of Rh ($\Phi \sim -4.98$ eV) and Ni ($\Phi \sim -5.15$ eV) can enhance the electric polarization of RhNi. Subsequently, the resulting RhNi is homogeneously distributed on top of the 2D nanostructure of the FeV_3O_8 support via another hydrothermal synthesis. Advanced analyses of the hydrothermally grown FeV_3O_8 @RhNi using transmission electron microscopy (TEM), density functional theory (DFT) calculations, and *in situ* synchrotron-based transmission-mode X-ray diffraction (XRD) indicate that the enhanced electric polarization of RhNi induces a desirable ohmic contact with FeV_3O_8 and an efficient intermolecular charge transfer between RhNi and the FeV_3O_8 support, reducing the activation energy for a transformation mechanism between Zn and ZnO. The resultant FeV_3O_8 @RhNi catalyst exhibits an outstanding electrocatalytic activity for ORR and OER, boasting a high half-wave potential (0.90 V) for the ORR and a low overpotential (120 mV) at 10 mA cm^{-2} for the OER. Furthermore, the FeV_3O_8 @RhNi electrode exhibits notably low overpotentials of 8 mV and 41 mV for the cathodic HER to achieve current densities of 10 and 100 mA cm^{-2} , respectively. When employed as both cathode and anode electrodes in an alkaline electrolyzer, the FeV_3O_8 @RhNi configuration yielded an impressive overall water splitting current density of 10 mA cm^{-2} at 1.44 V, which is much lower than conventional RuO_2 || Pt/C electrode (10 mA cm^{-2} at 1.66 V). In the rechargeable zinc-air battery, the FeV_3O_8 @RhNi air cathode demonstrates remarkable performance, maintaining a stable discharge-charge voltage gap of 0.79 V at 10 mA cm^{-2} , a specific capacity of 810 mAh g^{-1} , and life cycle stabilities of $>859 \text{ h}$ at 10 mA cm^{-2} . Notably, this proposed new class of FeV_3O_8 @RhNi catalysts proves successful in flexible Zn-air batteries,

exhibiting long-term stability for >198 h at 10 mA cm⁻².

2. Experimental

2.1. Synthesis of catalysts

2.1.1. Synthesis of the Ni-SA@Rh alloy (RhNi SAA)

For the synthesis of SAA, Ni(NO₃)₂·6 H₂O (2 mmol), polyvinylpyrrolidone (20 mg), ethylene glycol (8 mmol), hexadecyltrimethylammonium bromide (2 mmol), and Sodium borohydride (NaBH₄, 5 mL) were dissolved in citric acid (50 mL, 8.4 g) under magnetic stirring at room temperature for 4 h. Then, Rh(NO₃)₃ (2 mmol) dissolved in oleylamine (OAm, 6 mL), 1,2-dodecanediol (DDD, 100 mg), and Tetrabutylammonium hydroxide (TBAH, 200 µL) was added to the solution under magnetic stirring and the mixture was stirred at 40 °C for 1 h. The resultant reaction mixture was transferred into a Teflon-lined stainless steel autoclave and heated at 150 °C for 9 h. The resulting products were collected by centrifugation, washed with an ethanol/cyclohexane mixture, and dried. The product was annealed for 2 h in a furnace at 400 °C under a constant 10% H₂/N₂ flow at a heating rate of 2 °C min⁻¹ to yield the RhNi SAA. For comparison, Ni metal nanopowder was also synthesized following a similar procedure by mixing Ni(NO₃)₂·6 H₂O, polyvinylpyrrolidone, ethylene glycol, hexadecyltrimethylammonium bromide, and the NaBH₄ precursor.

2.1.2. Synthesis of FeV₃O₈ nanoplates

For the synthesis of FeV₃O₈ nanoplates, a solution was prepared by combining 0.01 mol of iron(II) nitrate (Fe(NO₃)₂·6 H₂O) and 0.03 mol of ammonium metavanadate (NH₄VO₃) with 90 mL of aqueous citric acid (C₆H₈O₇, 0.08 mol), maintaining a 1:3 mol ratio. This mixture was stirred using a magnetic stirrer. Subsequently, 20 mL of ethylene glycol (EG), 3 mmol of polyvinyl alcohol (PVA), and 0.003 mol of hexamethylenetetramine (HMTA) were added to the solution under magnetic stirring at 50 °C for 1 h. After cooling, the solution was allowed to degas at room temperature for 8 h. The resulting mixture was then heated with a ferrovanadium (FeV) seed layer-coated fluorine-doped tin oxide (FTO) substrate in a Teflon-lined stainless steel autoclave. This heating process occurred at 150 °C for 12 h, with a heating rate of 2 °C min⁻¹. The obtained sample was collected, washed with an ethanol/deionized water mixture, and dried under vacuum for 24 h. Finally, the sample was annealed for 5 h in a furnace at 550 °C at a heating rate of 2 °C min⁻¹, resulting in the formation of FeV₃O₈ nanoplates.

2.1.3. Dispersion of the RhNi SAAs on FeV₃O₈ nanoplates

The RhNi SAAs were dispersed on FeV₃O₈ nanoplates using a simple hydrothermal method. In a typical procedure, 25 mg of RhNi SAA powder was mixed with 18 mL of acetylacetone and 4 mL of terpinol. The resulting mixture was sonicated at room temperature for 45 min and then diluted in a mixture of ethanol and water (1:1). The resultant mixture was heated with the FeV₃O₈ nanoplate-coated FTO substrate for 12 h in a Teflon-lined stainless steel autoclave at 150 °C at a heating rate of 2 °C min⁻¹. The resulting samples were separated and washed three times using an ethanol/cyclohexane mixture (1:1). The final samples were annealed for 2 h in a furnace at 250 °C under a constant 10% H₂/N₂ flow at a heating rate of 2 °C min⁻¹ to yield FeV₃O₈@RhNi. The Ni metal nanopowder was dispersed on the FeV₃O₈ nanoplates under similar conditions to the RhNi SAA.

2.2. Material characterization and measurements details

Details of catalysts physicochemical characterization, electrochemical characterization and zinc-air batteries measurements are shown in [supporting information](#).

2.3. Computational details

The DFT calculations on Ni, Rh, and RhNi were conducted using the frozen-core projector augmented wave method encoded in the Vienna ab initio simulation package (VASP) and the generalized gradient approximations (GGA) and the Perdew–Burke–Ernzerhof (PBE) parametrization with a plane-wave-cut-off energy of 500 eV and a set of 80 k-point in the irreducible Brillouin zone. To understand the charge-transfer mechanism at the metal (Ni, Rh, or RhNi) and FeV₃O₈ interface, a representative (111) surface with 15 Å vacuum thickness was initially constructed for the Ni, Rh, and RhNi metal surfaces.

2.4. Assembly of flexible solid-state Zn–air battery

The flexible solid-state Zn–air battery was fabricated using a catalyst-coated carbon cloth (0.3-mm thickness, loading: 1.16 mg cm⁻²), polished Zn foil (dimension of 2.5 cm by 4.5 cm, 0.05-mm thickness), and polyvinyl alcohol (PVA)–KOH-based gel as the air cathode, anode, and electrolyte, respectively. The cathode was prepared using the same method as the air cathode in the Zn–air battery. The PVA–KOH-based gel electrolyte was prepared as follows: 5 g of PVA powder was dissolved into 50 mL of 6 M KOH under stirring at 90 °C to form a viscous solution, followed by casting onto a glass disk to form a thin polymer film. Then, the polymer film was frozen for 3 h at –25 °C in a freezer. The obtained PVA–KOH gel electrolyte was maintained at 0 °C for 3 h before the test. During the assembly of the solid-state Zn–air battery, the catalyst-coated carbon cloth cathode and polished Zn foil anode were placed on both sides of the PVA–KOH gel electrolyte (28-µm thick) and the glass fiber separator was placed between the air cathode and electrolyte. After assembling the interior, the solid-state Zn–air battery was sealed using the aluminum laminated materials with a hot press machine. The solid-state Zn–air battery cycling performance was measured using galvanostatic pulses for 10 min of discharge followed by 10 min of charge.

2.5. Assembly of pouch Zn–air battery

For assembly of the pouch Zn–air battery, a polypropylene-coated aluminum pouch was used as the packaging. The air-cathode side was perforated with pinholes to allow air to enter and exit. Afterward, a polytetrafluoroethylene (PTFE) film was attached to prevent leakage and evaporation of the electrolyte. To fabricate the pouch Zn–air battery, 0.2 M ZnC₄H₆O₄ containing 6 M KOH was used as the electrolyte. The FeV₃O₈@RhNi sample-coated GDL (areal mass loading: 1.18 mg cm⁻²) and a polished Zn plate (dimension of 3 cm by 4.5 cm, 0.2-mm thickness) were used as the cathode and anode, respectively. A glass fiber and aluminum strip were used as the separator and current collector, respectively. After assembling the interior, an electrolyte (1 mL) was injected into the separator and the pouch Zn–air battery was sealed using a hot press machine. The pouch Zn–air battery cycling performance was measured using galvanostatic pulses for 10 min of discharge followed by 10 min of charge.

2.6. In situ Raman spectra and synchrotron-based transmission-mode XRD analysis

To obtain the in-depth understanding of the Oxygen Evolution Reaction (OER), a series of in situ Raman experiments was conducted. A confocal Raman microscope (DXR, Thermo-Fisher Scientific) equipped with a 633 nm argon ion laser was employed for this purpose. The in situ Raman spectra were acquired from the FeV₃O₈@RhNi electrode, spanning potentials from 1.2 to 1.6 V versus the Reversible Hydrogen Electrode (RHE). Each spectrum was meticulously recorded with a duration of 45 seconds and intervals of 15 seconds. The FeV₃O₈@RhNi electrode was subjected to anodic scanning from 1.0 to 1.7 V at a constant rate of 1 mVs⁻¹ during data acquisition.

In situ transmission-mode XRD measurements were performed on the

Zn–air batteries with FeV_3O_8 and $\text{FeV}_3\text{O}_8\text{@RhNi}$ electrocatalysts at the 3 C beamline in the PAL, Pohang (South Korea) using a monochromatic X-ray radiation source of 31.4 keV (wavelength = 0.395 Å) and a 2D charge-coupled device (CCD) detector (Mar165 CCD). The Zn–air battery samples were vertically mounted on a z-axis goniometer, which allowed the incident X-ray beam to be transmitted to the body of Zn–air battery (termed transmission mode). 1 mL of 0.2 M $\text{ZnC}_4\text{H}_6\text{O}_4$ containing 6 M KOH was added to the cell as an electrolyte just before the measurement. The in situ battery cell were investigated under room temperature (25°C) and 1 atm condition. The samples were 0.201 m upstream from the CCD detector, and a current of –5 mA or +5 mA was applied for 6 h to the corresponding Zn–air battery for the discharge and charge modes, respectively.

3. Results and discussion

3.1. Catalysts fabrication and the intermolecular charge-transfer interaction

The RhNi single-atom alloy (SAA) catalyst was synthesized using a spontaneous co-reduction approach with $\text{Rh}(\text{NO}_3)_3$ and $\text{Ni}(\text{NO}_3)_2 \cdot 6\text{H}_2\text{O}$ as raw materials via a hydrothermal technique (Fig. 1a). NaBH_4 , DDD was used as the reducing agent and OAm was used as the coreducing agent and surfactant [67,68]. Owing to its powerful reduction capacity, it reduces the metals source in the precursor. The RhNi SAA composition

was tailored by adjusting the mole ratio of Rh^{III} and Ni^{II} . TBAH was utilized as a phase reagent to prevent the phase separation of Rh and Ni [69,70]. OAm not only induces nucleation for RhNi single-atom growth but also inhibits the growth of grains to construct the RhNi SAA. Furthermore, DDD and TBAH help to stabilize the RhNi SAA structure. Similarly, a homogenous solution was formed by dissolving EG, PVA, and HMTA in an aqueous $\text{C}_6\text{H}_8\text{O}_7$ mixture containing $\text{Fe}(\text{NO}_3)_3 \cdot 9\text{H}_2\text{O}$ and NH_4VO_3 , and then FeV_3O_8 was obtained using a hydrothermal technique. The obtained the RhNi SAA was dispersed over the FeV_3O_8 surface via a hydrothermal reaction; the product is denoted as $\text{FeV}_3\text{O}_8\text{@RhNi}$ (Fig. 1b). The weight ratio of metals in the synthesized samples were characterized using ICP–MS and are listed in Table S1, Supporting information. From the table, the stoichiometric ratio of Fe and V metal in FeV_3O_8 is 1:3. The Rh and Ni metal stoichiometric ratio of RhNi SAA content in the formed $\text{FeV}_3\text{O}_8\text{@RhNi}$ are 1:1, verifying successful dispersing of RhNi into FeV_3O_8 surface. The crystal structures of the FeV_3O_8 and $\text{FeV}_3\text{O}_8\text{@RhNi}$ catalysts were analyzed using XRD and grazing incident wide-angle X-ray scattering (GIWAX) (see Figs. S1 and S2, Supporting information for details).

To investigate the electric polarization of RhNi and its intermolecular interaction with FeV_3O_8 , DFT calculations were conducted to obtain electrostatic potential profiles for Ni, Rh, and RhNi. The calculated electrostatic potential profiles for Ni, Rh, and RhNi on the FeV_3O_8 surface exhibited positive electrostatic potentials across all systems, indicating a change in electric polarization (Fig. 1c). Notably, the RhNi alloy

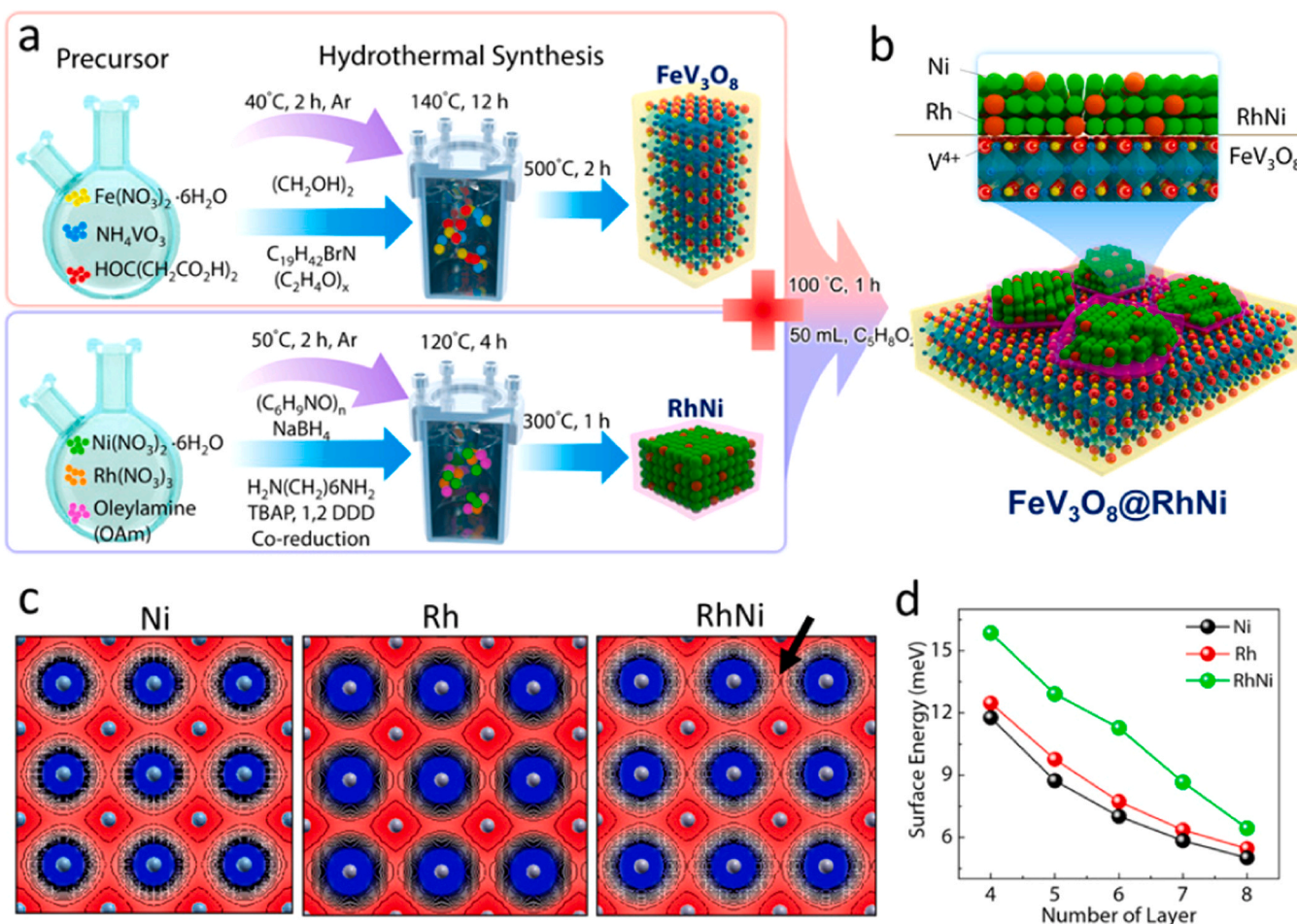


Fig. 1. Schematic of the catalyst synthesis processes and DFT calculations for $\text{FeV}_3\text{O}_8\text{@RhNi}$. a) Schematic illustrations of the synthesis of the FeV_3O_8 and RhNi alloy catalysts. b) Schematic illustration of the electrical polarization in RhNi, as well as the intermolecular interaction between FeV_3O_8 and RhNi caused by the charge-transfer mechanism. c) The electrostatic potential map calculated for the Ni, Rh, and RhNi surfaces. In the color map, the red and blue surfaces denote the positive and negative potentials, representing a condition of high and low electron density, respectively. The black arrow in RhNi indicates the presence of electric polarization. d) The calculated surface energy for Ni, Rh, and RhNi. The black, red, and green circles denote the Ni, Rh, and RhNi systems, respectively.

(marked by a black arrow) showed a highly dispersed and polarized electrostatic potential compared to that of pristine Ni and Rh. The polarized electric potential is mainly attributed to the higher electronegativity of the Rh *d*-state (2.28), compared to the Ni *d*-state (1.91) [71], which leads to different work functions and, thereby, an efficient charge transfer from Ni to Rh. The charge transfer within RhNi initiates an electric polarization effect, giving rise to a desirable intermolecular interaction with FeV₃O₈. Indeed, it was revealed that the FeV₃O₈ support acts as an electron acceptor at the interface between FeV₃O₈ and RhNi because the FeV₃O₈ support encompasses three distinct V ion types, resulting in its formulation as [Fe³⁺][V⁴⁺][V⁵⁺][V⁴⁺][O²⁻]₈ based on the electronic structure (see Fig. S3 and Supporting information for more details). In addition, surface energy calculations on Ni, Rh, and RhNi using the DFT method were performed to determine the degree of unsaturated coordination of the surface atoms (Fig. 1d). Notably, the large surface energy of RhNi indicates an intrinsically less energetically favorable and highly dynamic reactivity, which is directly related to electrocatalytic efficiency. Consistently, the RhNi alloy had the most elevated surface energy, indicating superior catalytic activity among the

aforementioned metal catalysts.

The local coordination environment of RhNi SAA is investigated by X-ray absorption near-edge structure (XANES). Fig. S4 shows the XANES L-edge curves of the RhNi SAA together with commercial Rh-foil and metallic Ni for comparison. In contrast to a monometallic Rh and Ni, RhNi SAA displayed variable white line intensity and pre-edge features of the Rh-L and Ni L3, 2-edge, as illustrated in Fig. S4. This might be attributed to both a strong electronic interaction between Rh and Ni and their altered coordination environments. Compared with the monometallic Rh and Ni, the Ni L-edge position of RhNi exhibited a slightly positive shift whilst the Rh L-edge position move to slight negative side, this could be the cause of electron transport from Ni metal to Rh atom in RhNi SAA.

Furthermore, the surface properties and RhNi SAA incorporation effect of the FeV₃O₈ catalyst were investigated by X-ray photoelectron spectroscopy (XPS) characterization. As shown in Fig. S5, representative XPS survey spectra of FeV₃O₈, RhNi single atom alloy and FeV₃O₈@RhNi show major characteristic peaks of Fe, V, Ni, Rh and O elements. The XPS measurements in the core-level Fe 2p and V 2p region

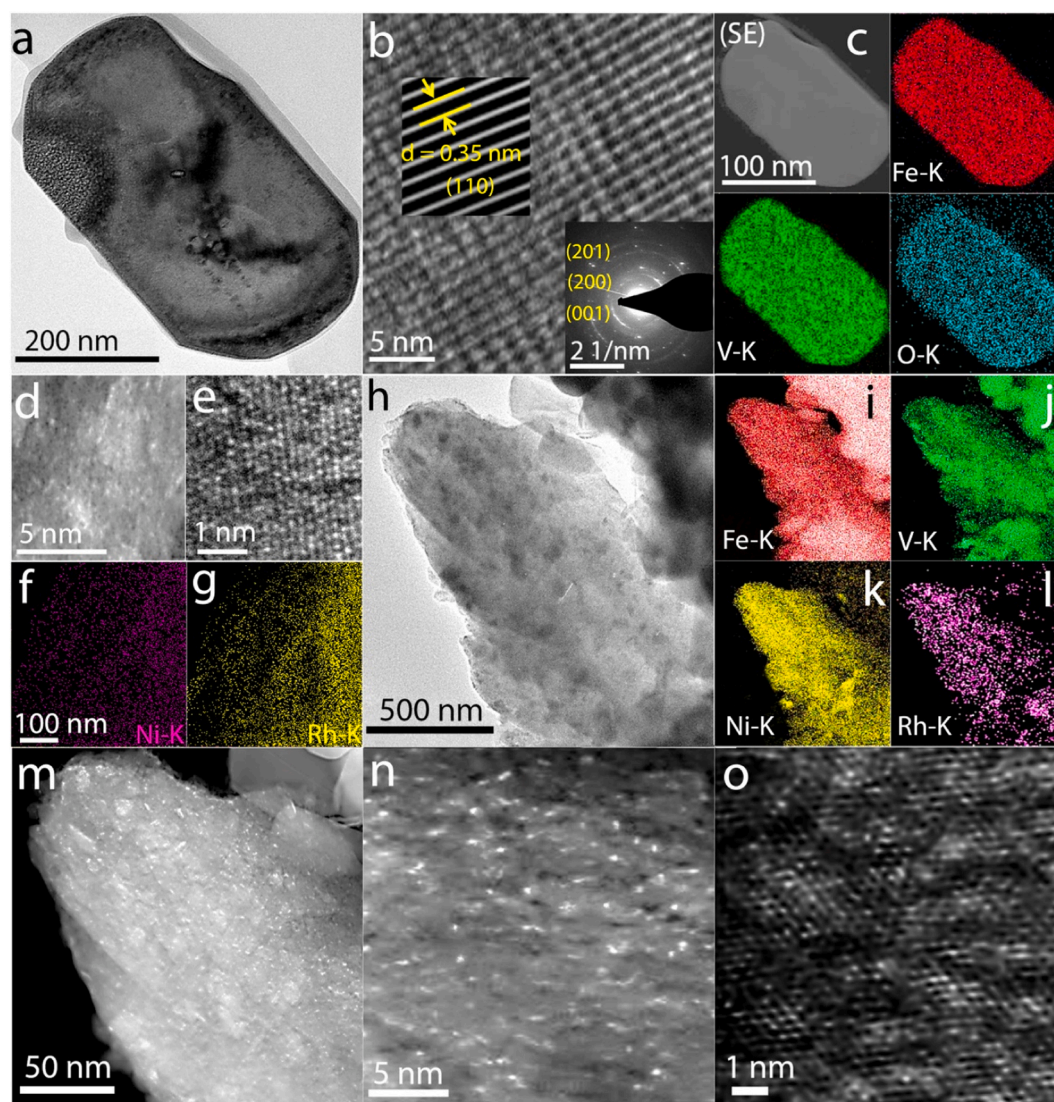


Fig. 2. Morphological characterizations of catalysts. a) TEM image of FeV₃O₈. b) HRTEM image and magnified image (inset) showing the lattice fringes of FeV₃O₈ and the corresponding SAED pattern in the lower corner. c) EDXS elemental mapping results of FeV₃O₈ showing the distribution of Fe, V, and O elements. d and e) AC HAADF-STEM images of RhNi. f and g) Corresponding elemental mapping images of Rh and Ni showing the uniform dispersion of Rh. h) HAADF-STEM images of FeV₃O₈@RhNi. i-l) EDXS mapping images of FeV₃O₈@RhNi showing the uniform dispersion of Fe, V, Rh, and Ni. m) HAADF-STEM images of FeV₃O₈@RhNi. n and o) AC HAADF-STEM images of FeV₃O₈@RhNi.

disclosed a strong electronic interaction between FeV_3O_8 and RhNi SAA. On $\text{FeV}_3\text{O}_8/\text{RhNi}$ data, we observed a downwards shift of Fe 2p and V 2p binding energies with compared to that of FeV_3O_8 , which is due to the charge transfer between RhNi and FeV_3O_8 (see Figs. S6a and S6b). This conclusion is confirmed by the core-level Rh 3d and Ni 2p XPS spectra of $\text{FeV}_3\text{O}_8/\text{RhNi}$. The enhanced binding energy shift for the spin-orbit peaks for both Rh 3d and Ni 2p in comparison with RhNi SAA suggests higher oxidation state of Rh and Ni (see Figs. S6c and S6d).

3.2. Morphology characterization of $\text{FeV}_3\text{O}_8/\text{RhNi}$

From the scanning electron microscopy (SEM, Figs. S7a and S7b) and transmission electron microscopy (TEM, Fig. 2a) measurements, we confirmed that the synthesized FeV_3O_8 samples had a nanoplate-like morphology. The high-resolution TEM (HR-TEM) image with (0.350 nm) lattice spacing of the (110) plane (Fig. 2b, upper inset) and the corresponding selected area electron diffraction (SAED) ring planes of (201), (200), (001) (Fig. 2b, lower inset) further confirmed the monoclinic phase of FeV_3O_8 with a polycrystalline nature (ICDD-

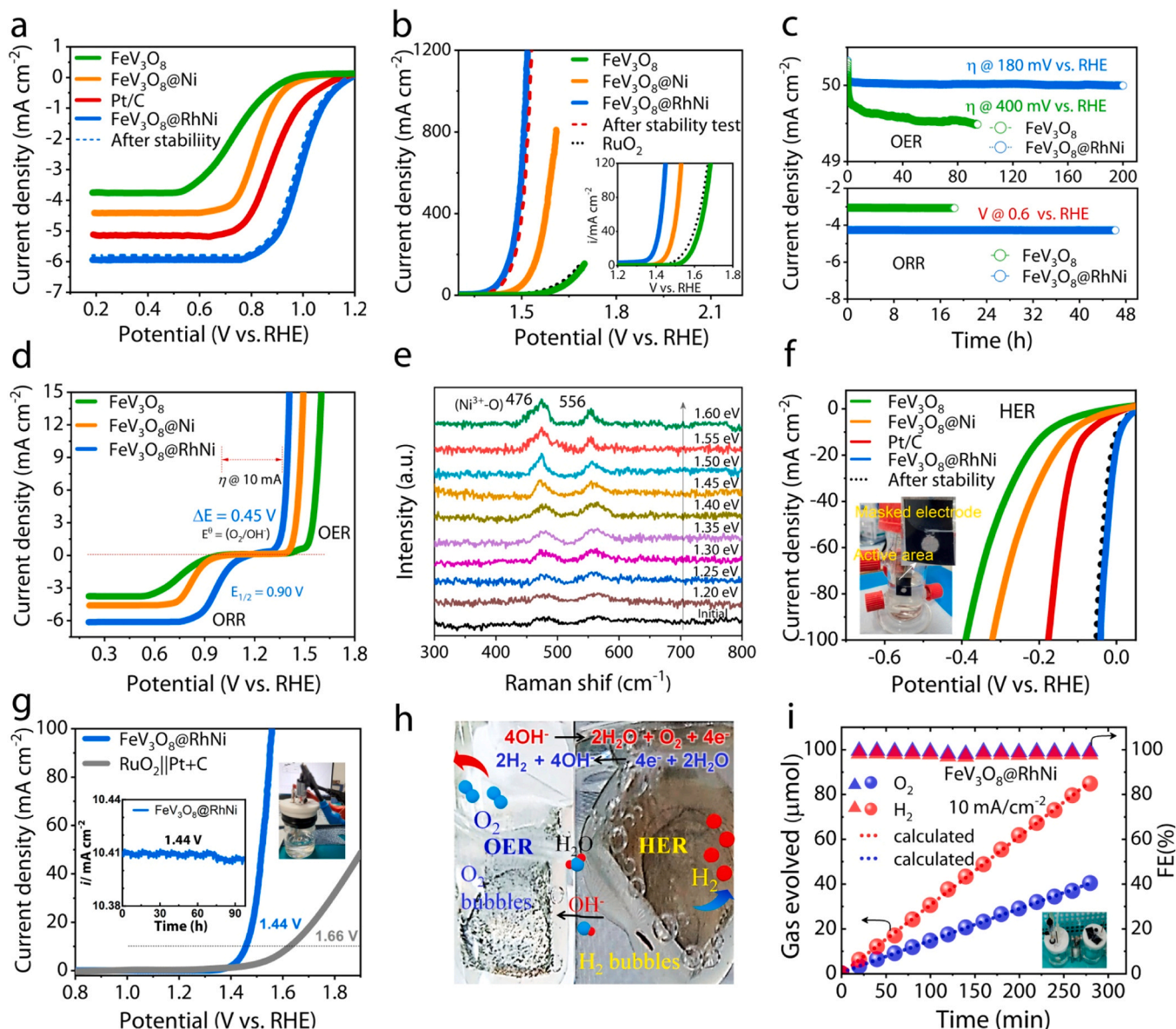


Fig. 3. Electrocatalytic properties of catalysts. a) ORR polarization curves for different catalysts recorded with a rotation rate of 1600 rpm in an oxygen-saturated 0.1 M KOH electrolyte at a scan rate of 5 mV s^{-1} . b) OER polarization curves of catalysts at a scan rate of 5 mV s^{-1} in 1 M KOH. The electrode diameters were 0.2 cm^2 . The dashed line (red) represents the chronoamperometric (OER) response of the $\text{FeV}_3\text{O}_8/\text{RhNi}$ catalyst. Inset shows enlarged LSV curves of the catalysts. c) Stability of the $\text{FeV}_3\text{O}_8/\text{RhNi}$ catalyst in the OER and ORR (@ 900 rpm) chronoamperometric (i - t) response measured at a constant potential compared with the FeV_3O_8 catalyst. d) ORR and OER polarization curves of the FeV_3O_8 , $\text{FeV}_3\text{O}_8/\text{Ni}$, and $\text{FeV}_3\text{O}_8/\text{RhNi}$ catalysts on an RDE at a rotation rate of 1600 rpm in an oxygen-saturated 0.1 M KOH electrolyte at a scan rate of 5 mV s^{-1} . The inset text shows the ΔE ($E_{j=10} - E_{1/2}$) of the $\text{FeV}_3\text{O}_8/\text{RhNi}$ catalyst. e) *In situ* Raman spectra of the $\text{FeV}_3\text{O}_8/\text{RhNi}$ electrode during a LSV scan from 1.20 to 1.7 V at a rate of 1 mV s^{-1} . f) HER polarization curves of the catalysts at a scan rate of 5 mV s^{-1} in 1 M KOH. The dotted line (black) represents the post chronoamperometric (HER) response of the $\text{FeV}_3\text{O}_8/\text{RhNi}$ catalyst. Inset photography shows the experimental set-up for the HER measurement. g) Polarization curve for overall water splitting of the $\text{FeV}_3\text{O}_8/\text{RhNi}$ catalyst compared with a commercial $\text{RuO}_2 + \text{Pt/C}$ catalyst. Insets show the chronoamperometric (i - t) response of the $\text{FeV}_3\text{O}_8/\text{RhNi}$ catalyst in the overall water splitting measured at 1.44 V and experimental set-up. h) Photographic evidence of O_2 and H_2 evolution of the $\text{FeV}_3\text{O}_8/\text{RhNi}$ catalyst at a current density of 10 mA cm^{-2} . i) The experimentally measured (GC) and theoretically calculated O_2 and H_2 evolution rate with Faradaic efficiency (%) of the $\text{FeV}_3\text{O}_8/\text{RhNi}$ catalyst at 10 mA cm^{-2} (the experimental GC set-up shown in the inset).

01–075–0811). The SEM energy-dispersive X-ray spectroscopy (EDXS) (Figs. S7c and S7d), and corresponding TEM–EDXS elemental mapping across a single FeV_3O_8 nanoplate (Fig. 2c) showed a homogeneous distribution of Fe and V. Fig. 2d and Fig. S8a in the Supporting information show the aberration-corrected (AC) high-angle annular dark-field scanning TEM (HAADF–STEM) images of RhNi. Owing to the higher Z value of Rh than Ni, bright dots were observed in the AC HAADF–STEM images (Fig. 2e), suggesting that Rh atoms were atomically distributed on the Ni nanoparticles. The EDXS mapping (Figs. 2f, 2g, and Figs. S8b, S9) also revealed the homogeneous distribution of Rh atoms on the Ni nanoparticles. The SEM images and EDS mapping of $\text{FeV}_3\text{O}_8/\text{RhNi}$ is shown in supplemental information (Fig. S10). Moreover, for a single $\text{FeV}_3\text{O}_8/\text{RhNi}$ nanoplate, the corresponding HR–TEM images and EDXS mapping images revealed that the Ni and Rh atoms comprising the nanoparticle were uniformly dispersed over the entire plate, confirming that the RhNi SAAs were embedded on top of FeV_3O_8 (Figs. 2h–2l and 2m). Using Z-contrast analysis on the AC HAADF–STEM images (Figs. 2n and 2o), we found that brighter spots indicated isolated Rh single atoms on the FeV_3O_8 surface due to their higher atomic number.

3.3. Electrocatalytic performance of $\text{FeV}_3\text{O}_8/\text{RhNi}$ for ORR and OER

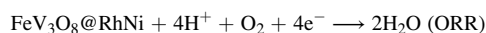
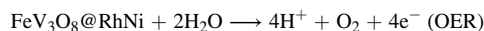
To investigate the effects of Ni, Rh, and RhNi on the electrocatalytic performance of FeV_3O_8 , their ORR activities were initially assessed using cyclic voltammetry (CV) in oxygen (O_2)- and nitrogen (N_2)-saturated 0.1 KOH. The $\text{FeV}_3\text{O}_8/\text{RhNi}$ catalyst exhibited a higher active polarization curve with the most positive onset potential of 1.15 V compared to $\text{FeV}_3\text{O}_8/\text{Ni}$ (1.0 V) and FeV_3O_8 (0.90 V) (Fig. S11). The linear sweep voltammetry (LSV) curve (Fig. 3a) of $\text{FeV}_3\text{O}_8/\text{RhNi}$ delivered a half-wave potential of 0.90 V and reached a limiting current density of -5 mA cm^{-2} , which were higher than those of FeV_3O_8 (0.46 V and -3.5 mA cm^{-2} , respectively) and $\text{FeV}_3\text{O}_8/\text{Ni}$ (0.65 V and -4 mA cm^{-2} , respectively). These results were also higher than those of benchmark Pt/C (0.74 V and -4.5 mA cm^{-2} , respectively) and previously reported single atom-based electrocatalysts (Tables S2 and S3), corroborating that the RhNi SAAs on the FeV_3O_8 surface greatly enhanced ORR performance. The Tafel slope of $\text{FeV}_3\text{O}_8/\text{RhNi}$ (32 mV dec^{-1}) was much lower than that of Pt/C (62 mV dec^{-1}), whereas $\text{FeV}_3\text{O}_8/\text{Ni}$ (86 mV dec^{-1}) and FeV_3O_8 (166 mV dec^{-1}) exhibited higher Tafel slopes, revealing that the FeV_3O_8 and the RhNi SAA conjugation effectively improved the inherent kinetics activity (Fig. S12). The ORR reaction mechanism and the number of electron transfer per oxygen molecule (n) of the catalysts were evaluated using the Koutecký–Levich (K–L) equation. The K–L plots of catalysts at different potential shows good linear and parallel characteristics (Fig. S13), revealing that the ORR process is a typical first-order reaction [72]. The n values of FeV_3O_8 and $\text{FeV}_3\text{O}_8/\text{RhNi}$ were 3.9 and 4, respectively, indicating a four-electron pathway for ORR [73]. The n and H_2O_2 evolution yield during the ORR process were further investigated using the rotating ring-disk electrode (RRDE) technique, which confirmed the direct four-electron path ORR process (Fig. S14) [74]. The H_2O_2 evolution yield was $<2.1\%$, confirming the selectivity of direct O_2 reduction to OH^- [75,76]. The methanol tolerance of the $\text{FeV}_3\text{O}_8/\text{RhNi}$ catalyst was examined; the results showed that there was almost no change in the ORR current compared to Pt/C (Fig. S15).

The OER performances of the RuO_2 , FeV_3O_8 , $\text{FeV}_3\text{O}_8/\text{Ni}$, and $\text{FeV}_3\text{O}_8/\text{RhNi}$ electrocatalysts were also investigated in 1 M KOH. The LSV polarization curves demonstrated that $\text{FeV}_3\text{O}_8/\text{RhNi}$ exhibited sharp increases in the anodic current response, with overpotentials of 120 mV and 200 mV at current densities of 10 and 100 mA cm^{-2} , respectively. These overpotentials were lower than those of $\text{FeV}_3\text{O}_8/\text{Ni}$ (250 and 290 mV, respectively), FeV_3O_8 (360 and 450 mV, respectively), and commercial RuO_2 (330 and 420 mV, respectively) and considerably lower than previously reported single atom-based OER electrocatalysts (Fig. 3b and Tables S3 and S4). The superior OER activity of $\text{FeV}_3\text{O}_8/\text{RhNi}$ was further corroborated by the lowest Tafel

slope (42 mV dec^{-1}) when compared to FeV_3O_8 (115 mV dec^{-1}), $\text{FeV}_3\text{O}_8/\text{Ni}$ (69 mV dec^{-1}), and RuO_2 (93 mV dec^{-1}), indicating rapid OER kinetics (Fig. S16). We further investigated the intrinsic properties of the catalysts. $\text{FeV}_3\text{O}_8/\text{RhNi}$ had (η @ 270 mV) a much higher turnover frequency (TOF) 0.23780 s^{-1} than $\text{FeV}_3\text{O}_8/\text{Ni}$ (0.02096 s^{-1}) and FeV_3O_8 (0.000483 s^{-1}). Importantly, the electrochemically active surface area (ECSA) of $\text{FeV}_3\text{O}_8/\text{RhNi}$ was nearly four times (130 cm^2) higher than that of FeV_3O_8 (35 cm^2), demonstrating that decoration with the RhNi SAA considerably improved the intrinsic properties of FeV_3O_8 (see Fig. S17 and Table S4 in the Supporting information for details).

The ORR and OER stability of the FeV_3O_8 and $\text{FeV}_3\text{O}_8/\text{RhNi}$ catalysts were further examined using chronoamperometric analysis (Fig. 3c). There was no obvious degradation of $\text{FeV}_3\text{O}_8/\text{RhNi}$ after continuous ORR catalysis for 46.6 h (0.6 V vs. RHE @ 900 rpm), whereas the stability of pristine FeV_3O_8 and $\text{FeV}_3\text{O}_8/\text{Ni}$ (Fig. S18) was as low as 18.8, and 21.9 h, respectively. In addition, the post SEM (Fig. S19) and inductively coupled plasma mass spectrometry (ICP–MS) analysis (Table S5) revealed that changes in morphology and metal ion leaching were not detected in the KOH solution during the ORR stability test, indicating that the strong intermolecular interaction of FeV_3O_8 and the RhNi SAA increased the ORR stability. For the OER stability, the initial OER current density of the FeV_3O_8 and $\text{FeV}_3\text{O}_8/\text{Ni}$ (Fig. S20) catalyst decreased by 8% and 5% after 95.4 and 111.5 h, whereas the polarization current of the $\text{FeV}_3\text{O}_8/\text{RhNi}$ catalyst remained almost constant for >201.4 h without changing the stoichiometry and morphology (Fig. S21 and Table S6).

Owing to the excellent ORR and OER performances, the overall oxygen electrode activities of the catalysts were further estimated. The difference between the OER and ORR potentials ($\Delta E = E_{\text{OER}} - E_{\text{ORR}}$) in 0.1 M KOH can be used to assess the bifunctional oxygen catalytic activity. When the synthesized catalyst has a lower ΔE value, it is more suitable for use as a bifunctional oxygen catalyst in metal–air batteries [77–79]. Therefore, the bifunctional oxygen catalytic activity of the catalysts was analyzed in an O_2 -saturated 0.1 M KOH solution at a rotation speed of 1600 rpm. The $\text{FeV}_3\text{O}_8/\text{RhNi}$ catalyst exhibited a low ΔE of 0.45 V, which was lower than those of $\text{FeV}_3\text{O}_8/\text{Ni}$ ($\Delta E = 0.68 \text{ V}$), FeV_3O_8 ($\Delta E = 0.88 \text{ V}$), and reported bifunctional and single atom-based bifunctional electrocatalysts (Fig. 3d and Fig. S22 and Tables S3 and S7), demonstrating the high oxygen catalytic activity of the $\text{FeV}_3\text{O}_8/\text{RhNi}$ catalyst. Based on the aforementioned experimental results, the electrochemical OER and ORR reaction in the $\text{FeV}_3\text{O}_8/\text{RhNi}$ is illustrated in following equation [80,81].



As noticed in the XPS and TEM analysis, the dispersion of the RhNi SAAs on the FeV_3O_8 surface generated isolated atomic Rh, which is a feasible catalytic site for ORR [82]. On the other hand, the high oxidation states of RhO and RhO_2 can accelerate water oxidation by effectively removing surface holes [83]. The presence of Ni^{3+} ions in alkaline solutions is known to generate $\text{Ni}^{3+}(\text{O})\text{-OH}$ intermediates, which subsequently react with hydroxide ions to produce oxygen molecules [84]. On the surface of the $\text{FeV}_3\text{O}_8/\text{RhNi}$ catalyst, the existence of Ni^{3+} facilitates electrostatic adsorption of OH^- and reduces the energy barrier for breaking the O–H bond and forming the O–O bond. This simplifies the conversion of $^*\text{OH}$ to $^*\text{O}$ species in the Oxygen Evolution Reaction (OER) [85,86]. To identify the active catalytic species involved in the OER under KOH conditions, potential-dependent in-situ Raman experiments were conducted on a $\text{FeV}_3\text{O}_8/\text{RhNi}$ electrode. As depicted in Fig. 3e, at potentials below 1.25 V vs RHE, in-situ Raman spectra exhibit no significant changes. However, at applied potentials ranging from 1.25 to 1.6 V vs RHE, the intensities of bands at 476 and 556 cm^{-1} , corresponding to the bending and stretching vibration modes of NiOOH , gradually increase. This analysis suggests that NiOOH generated during

the OER is likely the catalytically active species on the FeV₃O₈@RhNi electrode [87,88].

Hence, it is hypothesized that H₂O preferably adsorbs on Ni³⁺ sites before sequentially dissociating into atomic oxygen species (H₂O → OH → O), while released H intermediates prefer to adsorb on Rh sites rather than Ni³⁺ sites. Consequently, Rh sites are crucial for dehydrogenating H₂O and OH, facilitating the formation of O intermediates on Ni³⁺ sites. This indicates that Ni and Rh play significant roles in the adsorption of oxygen and hydrogen intermediates, respectively, synergistically aiding in H₂O dissociation and subsequent dehydrogenation processes during the OER. Additionally, the alloyed single-atom Rh and Ni species in the RhNi heterojunction enhance electron transfer and OER kinetics. Consequently, the overpotential (@10 mA cm⁻²) and Tafel slope of FeV₃O₈@RhNi were significantly lower compared to those of FeV₃O₈ and FeV₃O₈@Ni.

3.4. Electrocatalytic performance of FeV₃O₈@RhNi for HER and overall water splitting

To further explore the FeV₃O₈@RhNi as multifunctional electrocatalysts, we examined their activity for HER. The performances were analyzed in 1 M KOH solutions. FeV₃O₈@RhNi exhibited remarkable HER activity, which was better than those of the reference 20 wt% Pt/C catalyst, FeV₃O₈@Ni, and FeV₃O₈ (Fig. 3f). The overpotentials to reach 10 and 100 mA cm⁻² were only 8 and 41 mV for FeV₃O₈@RhNi, which were lower than those of Pt/C, FeV₃O₈@Ni, FeV₃O₈, and other state-of-the-art single-atom catalysts in alkaline media (see Table S8). The excellent HER activity of FeV₃O₈@RhNi was further demonstrated (Fig. S23) by the lower Tafel slope (29 mV dec⁻¹) compared to Pt/C (48 mV dec⁻¹), FeV₃O₈@Ni (111 mV dec⁻¹) and FeV₃O₈ (166 mV dec⁻¹) suggesting that the rapid HER kinetics followed the Volmer–Tafel pathway [89,90] according to the following steps: H₂O + e⁻ → H_{ads} + OH⁻ (the water decomposition, Volmer), H_{ads} + H_{ads} → H₂ (hydrogen formation step Tafel) and the rate-determining step is the chemical recombination of absorbed hydrogen. As expected, the presence of RhNi SAA sites may act synergistically to enhance the catalytic activity for HER. On the surface of RhNi SAA, hydroxide ions (OH⁻) generated from water splitting tend to preferentially attach to positively charged Ni²⁺ and Ni³⁺ sites, forming Ni-OH species. Meanwhile, neighboring Rh single-atom sites play a significant role in hydrogen (H) adsorption. This synergistic interaction between Rh and Ni is crucial for promoting the rate-determining step of HER, known as the Volmer step [91,92]. In contrast, the FeV₃O₈@Ni surface exhibits low activity for HER, necessitating higher applied potentials due to the absence of Rh sites for hydrogen adsorption. Consequently, adsorbed OH⁻ species may occupy potential hydrogen adsorption sites, leading to inefficient OH⁻ release and the blocking of active catalytic sites. This observation suggests a positive influence of RhNi SAA on both water adsorption and dissociation processes on the FeV₃O₈@RhNi catalyst surface. Furthermore, the nanostructured 2D FeV₃O₈ plate, with its high surface area, provides a large contact area and strong interaction, effectively serving as a host-guest platform for the HER-active RhNi SAA. Additionally, the LSV polarization curves (Fig. 3f, black dotted lines) of FeV₃O₈@RhNi show nearly overlapping behavior before and after 45 hours of continuous chronoamperometric testing at an overpotential of 38 mV (Fig. S24), indicating excellent HER stability of FeV₃O₈@RhNi in 1 M KOH.

Inspired by the high catalytic activity of FeV₃O₈@RhNi for OER and HER in 1 M KOH, we constructed a full electrolyzer cell with FeV₃O₈@RhNi as the anode and cathode for overall water splitting (Fig. 3g). The electrolyzer using FeV₃O₈@RhNi as the electrode delivered a current density of 10 mA cm⁻² at 1.44 V, which outperformed the RuO₂ || Pt/C electrode (10 mA cm⁻² at 1.66 V). The stability test for overall water splitting was evaluated using continuous chronoamperometric measurements in 1 M KOH at 1.44 V. The FeV₃O₈@RhNi electrode provided a good level of stability by maintaining 10 mA cm⁻² for >90 h (Fig. 3g, inset). Furthermore, O₂ and H₂ bubbling (Fig. 3h) was

observed on the surface of the assembled electrodes during overall water splitting, revealing the high efficiency of the FeV₃O₈@RhNi electrode [93]. Moreover, the O₂ and H₂ evolution rates corresponding to the Faradaic efficiency (FE) (%) of the FeV₃O₈@RhNi electrocatalyst as a function of time is shown in Fig. 3i, demonstrating a nearly 100% FE of the FeV₃O₈@RhNi-based water splitting system.

3.5. Probing the intermolecular charge-transfer interaction in FeV₃O₈@RhNi

To identify how RhNi single atoms interact with FeV₃O₈ for superior bifunctional performance, synchrotron-based K-edge X-ray absorption near-edge structure (XANES) spectroscopy was performed (Fig. 4a). The Rh adsorption energies of the RhNi SAA and FeV₃O₈@RhNi catalysts were between those of Rh-foil and Rh₂O₃ references, indicating that metallic and oxidized Rh species coexist (Fig. 4a, inset). The Rh adsorption pre-edge positions of the RhNi SAA and FeV₃O₈@RhNi catalysts were lower than that of Rh₂O₃, indicating that the valence states of Rh in the RhNi SAA and FeV₃O₈@RhNi were lower than that in the Rh₂O₃ reference. Furthermore, FeV₃O₈@RhNi exhibited substantially weaker white line intensity than the RhNi SAA and the Rh₂O₃ reference, demonstrating the unsaturated coordination of Rh atoms in FeV₃O₈@RhNi [94]. In addition, the K²-weighted Fourier-transformed extended X-ray absorption fine structures (FT-EXAFS) of Rh are shown in Fig. 4b. The RhNi alloy sample exhibited a major peak at 2 Å attributed to the Rh–Ni bond, which was shorter than the Rh–Rh peak at 2.54 Å for the Rh-foil and larger than the Rh–O peak at 1.48 Å for Rh₂O₃. This confirms that the Rh atoms were surrounded by Ni to form the RhNi alloy [94,95]. FeV₃O₈@RhNi exhibited a dominant peak at 1.75 Å, which was located between the Rh–O peak at 1.48 Å for Rh₂O₃ and the Rh–Ni peak at 2 Å for the RhNi SAA. Therefore, this is explained by a combination of Rh–O and Rh–Ni bonding [96]. Furthermore, no Rh–Rh bond was observed in both RhNi and FeV₃O₈@RhNi, confirming the atomic nature of the Rh species [97,98] in both the catalysts, which is consistent with the AC HAADF-STEM results.

The normalized Ni K-edge XANES spectra of FeV₃O₈ and FeV₃O₈@RhNi exhibited a slightly more positive shift than the Ni-foil reference, indicating the presence of oxidized Ni species in RhNi and FeV₃O₈@RhNi (Fig. 4c). The enhanced intensity white line of FeV₃O₈@RhNi compared with RhNi further indicated the change in electron density and coordination environment of Ni species after the dispersion of RhNi on FeV₃O₈. The Ni–Ni and Ni–Rh bands can be identified by the prominent peaks in the FT-EXAFS spectra, which were observed at approximately 2.6 Å and 1.86 Å, respectively, for the RhNi SAA and 2.65 Å and 1.72 Å, respectively, for FeV₃O₈@RhNi (Fig. 4d). More importantly, the peak from the Ni–Rh contribution for FeV₃O₈@RhNi shifted to a lower value compared to the RhNi SAA, which could be the result of the RhNi dispersion on FeV₃O₈ creating a local symmetry structural distortion [99]. The simultaneous emergence of a Ni–O peak at 1.38 Å, which was absent in the RhNi SAA, confirmed that additional Ni–O coordination had formed in FeV₃O₈@RhNi [100]. Figs. S25 and S26 in the supporting information show the Fe and V K-edge XANES spectra of FeV₃O₈ and FeV₃O₈@RhNi, as well as the references. Compared to FeV₃O₈, the pre-edge intensity and white line features in the Fe and V K-edge XANES spectra of FeV₃O₈@RhNi were positively shifted after dispersing RhNi on FeV₃O₈, which matched well with the corresponding X-ray photoelectron spectroscopy (XPS) Fe 2p and V 2p spectra results. The formation of the interface between the RhNi SAA and FeV₃O₈ was further corroborated by the HRTEM and EDXS elemental mapping images (Fig. S27, S28, and S29). The above results confirmed the successful formation of the RhNi–FeV₃O₈ interface with a unique combination of the RhNi SAA and FeV₃O₈ electrocatalyst.

The normalized O K-edge XANES spectra were examined to estimate the oxygen vacancies of the FeV₃O₈@RhNi sample compared to FeV₃O₈ and the RhNi SAA (Fig. 4e). The O K-edge XANES spectra for the FeV₃O₈ and FeV₃O₈@RhNi samples featured three peaks marked as A, B, and C.

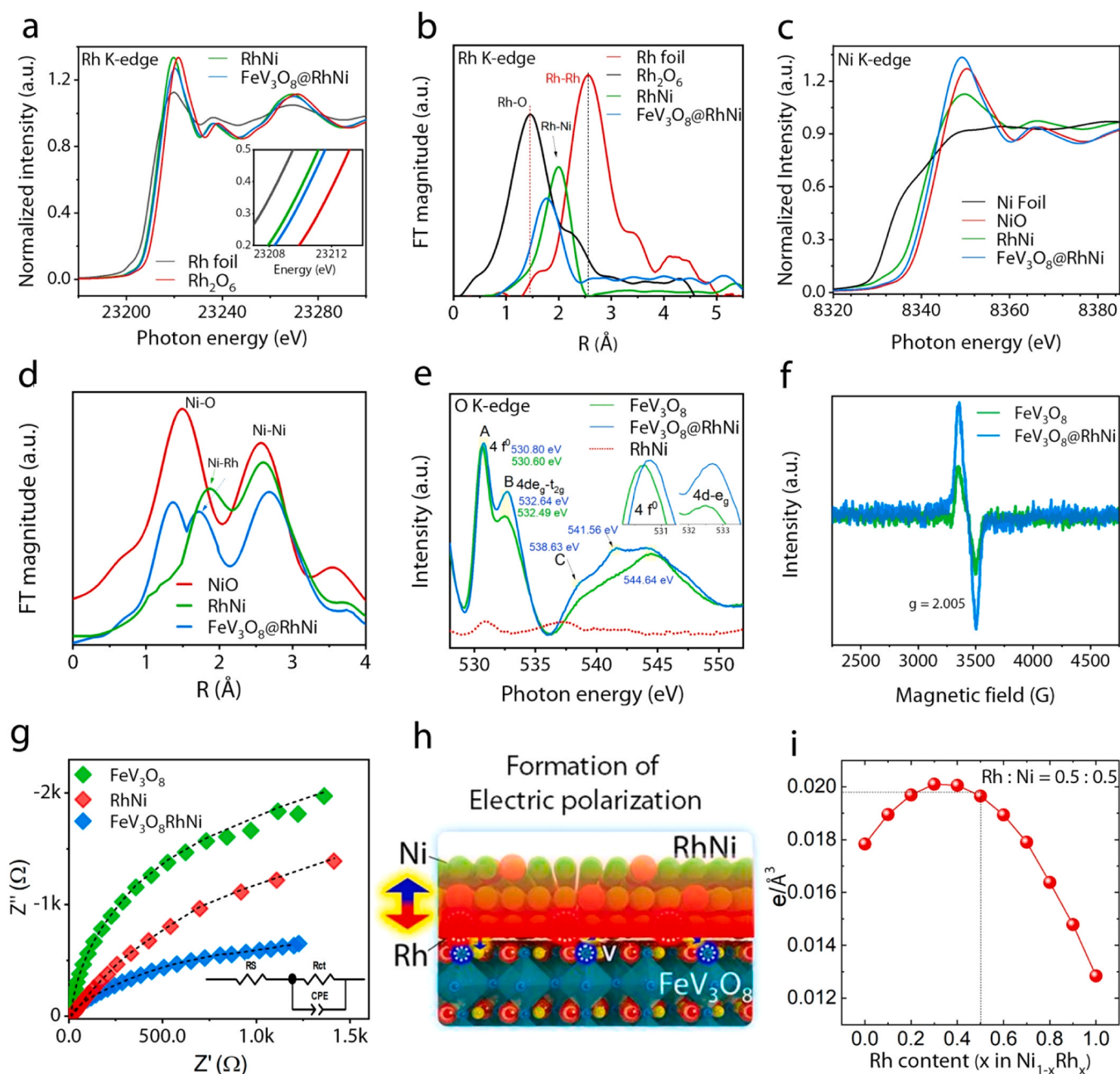


Fig. 4. Structural, electrical, and ESR properties of the catalysts. a) The Rh K-edge XANES spectra of RhNi, $\text{FeV}_3\text{O}_8\text{@RhNi}$, Rh_2O_3 , and Rh-foil. b) FT-EXAFS spectra for the Rh K-edge of RhNi, $\text{FeV}_3\text{O}_8\text{@RhNi}$, Rh_2O_3 , and Rh-foil. c) Ni K-edge XANES spectra of RhNi and $\text{FeV}_3\text{O}_8\text{@RhNi}$ compared with the standard Ni^{II}O and Ni-foil. d) FT-EXAFS spectra for Ni K-edge of RhNi, $\text{FeV}_3\text{O}_8\text{@RhNi}$, and NiO. e) O K-edge XANES spectra of FeV_3O_8 , $\text{FeV}_3\text{O}_8\text{@RhNi}$, and RhNi. f) EPR profile of the FeV_3O_8 and $\text{FeV}_3\text{O}_8\text{@RhNi}$ catalysts. g) EIS spectra (Nyquist plots) of the various catalysts measured in a three-electrode configuration in 1 M KOH (inset, equivalent circuit). h) Schematic image for a formation of electrical polarization of RhNi on FeV_3O_8 originated from the difference of charge density between Rh and Ni. i) The variation in relative charge density between the surface and centered metal layer as a function of Rh-content via DFT calculations.

FeV_3O_8 and $\text{FeV}_3\text{O}_8\text{@RhNi}$ exhibited a sharp peak at 530 eV, which was assigned to the transition between the O 1s and O 2p states hybridized with the metal 4 f^0 state, mainly localized at the metal site [101]. The intense peak around 532 eV and the $\text{FeV}_3\text{O}_8\text{@RhNi}$ spectra peak around 538 eV may represent the hybridization of O 2p states and metal 4 d_{eg-t_2g} molecular orbitals [102,103]. The weak O K-edge peak intensities of $\text{FeV}_3\text{O}_8\text{@RhNi}$ around 541 and 544 eV suggested local electronic hybridization of metal and oxygen [104]. The changes in peak A indicated variations in the hybridization of O 2p-metal 4 f states and affected the 4 f site occupancy, which could be associated with the valance of the metal ions [105]. Peaks B and C were directly related to the local crystal structure changes [104]. Additionally, it has been reported

that increases in peaks B are directly correlated to oxygen vacancy ordering in nonstoichiometric metal oxides [106].

To further investigate the effect of the RhNi SAA dispersion on the local atomic structure of $\text{FeV}_3\text{O}_8\text{@RhNi}$, electron paramagnetic resonance (EPR) measurements were performed on the corresponding sample. The EPR spectrum of $\text{FeV}_3\text{O}_8\text{@RhNi}$ showed a higher resonance signal at $g = 2.005$ than FeV_3O_8 , demonstrating the unpaired electron and higher oxygen vacancy [107] in $\text{FeV}_3\text{O}_8\text{@RhNi}$, which was consistent with the XANES (O K-edge) and XPS (O1s) results (Fig. 4f, Fig. S30 and Table S9). This was attributed to the formation of distinctly coordination-unsaturated local environment during the strong interfacial interaction between RhNi and FeV_3O_8 [108,109]. Moreover, to

investigate the charge-transfer properties of the electrocatalysts, electrochemical impedance spectroscopy (EIS) measurements were performed at the open circuit potential (OCP) versus RHE in 1 M KOH. The Nyquist plots are shown in Fig. 4g (see also the circuit (Figs. S31 and S32) and fitting parameters (Table S10). $\text{FeV}_3\text{O}_8/\text{RhNi}$ demonstrated a charge-transfer resistance (R_{ct}) of 311 Ω , which was lower than those of FeV_3O_8 (1965 Ω) and the RhNi SAA (920 Ω), suggesting that the RhNi SAA synergistic effects with FeV_3O_8 contributed to the enhanced charge transport ability of $\text{FeV}_3\text{O}_8/\text{RhNi}$. The specific surface area and porous nature of FeV_3O_8 and $\text{FeV}_3\text{O}_8/\text{RhNi}$ were examined using Brunauer–Emmett–Teller (BET) adsorption–desorption isotherms. The BET isotherms and pore distribution curve indicated that the $\text{FeV}_3\text{O}_8/\text{RhNi}$ catalyst exhibited a higher surface area and porous structure than FeV_3O_8 (Fig. S33 and Table S11).

Based on the results above, we proposed a formation mechanism of electric polarization at the RhNi surface as shown schematically in Fig. 4h. Owing to the $\Delta\phi$ in the RhNi alloy, where Rh has a higher surface electron density than Ni, the asymmetric nature of the charge polarization of RhNi can induce electrical polarization. To probe the formation of electrical polarization on RhNi surface, we investigated the relative charge density difference of the Rh and Ni surface as a function of Rh-content (x), which is associated with the charge density of the centered metal layer (Fig. 4i). The higher charge density difference indicates that the charge density on the metal surface becomes more polarized, leading to the formation of strong electric polarization. Hence, we found that the development of electric polarization is maximized at approximately $x = 0.5$ because the difference in charge density between the surface and the centered metal layer gradually increases in $x = \sim 0.5$ (Rh-content), and then decrease with a parabolic relationship as the Rh-content is approaching $x = 1.0$. The findings suggested that the

formation of a RhNi alloy with a balanced ratio of 0.5:0.5 is imperative for improving both electric polarization and electrochemical reaction activity. Notably, this ratio was used for the experimental conditions in our study. Moreover, we would also suggest that the formation of electric polarization on RhNi can induce severe band bending to establish a desirable ohmic contact with FeV_3O_8 because the ϕ of FeV_3O_8 (~ -5.50 eV) is higher than the $\Delta\phi$ in RhNi (Supporting Information Fig. S34, Energy Band diagram). Hence, the polarization-enhanced ohmic contact in $\text{FeV}_3\text{O}_8/\text{RhNi}$ allows an efficient charge transfer from RhNi to FeV_3O_8 , dramatically improving the electrocatalytic efficiency.

3.6. DFT calculation for the energy profiles of reaction pathways and adsorption energy in $\text{FeV}_3\text{O}_8/\text{RhNi}$

To elucidate the underlying mechanisms governing electrochemical reactions in $\text{FeV}_3\text{O}_8/\text{RhNi}$, including ORR, OER, and HER, we conducted an extensive analysis of adsorption energies using Density Functional Theory (DFT) calculations for each reaction pathway. Specifically, this investigation focuses on evaluating the influence of electric polarization of RhNi on the variation of adsorption energies during the electrochemical reactions. The study initially delineated the M-O, M-OH, M-OOH, M-O₂, and M-H₂O processes utilizing the Vienna Ab initio Simulation Package (VASP) software within the generalized gradient approximation (GGA) framework, where M represents RhNi, O denotes an Oxygen atom, OOH signifies hydroperoxide, O₂ represents oxygen, and H₂O denotes a water molecule as shown in Fig. 5a. Notably, the change of Rh content (x) within RhNi ranging from $x = 0.0$ to $x = 1.0$, achieved via the Virtual Crystal Approximation (VCA) method, was incorporated into the VASP calculations. Consequently, distinct

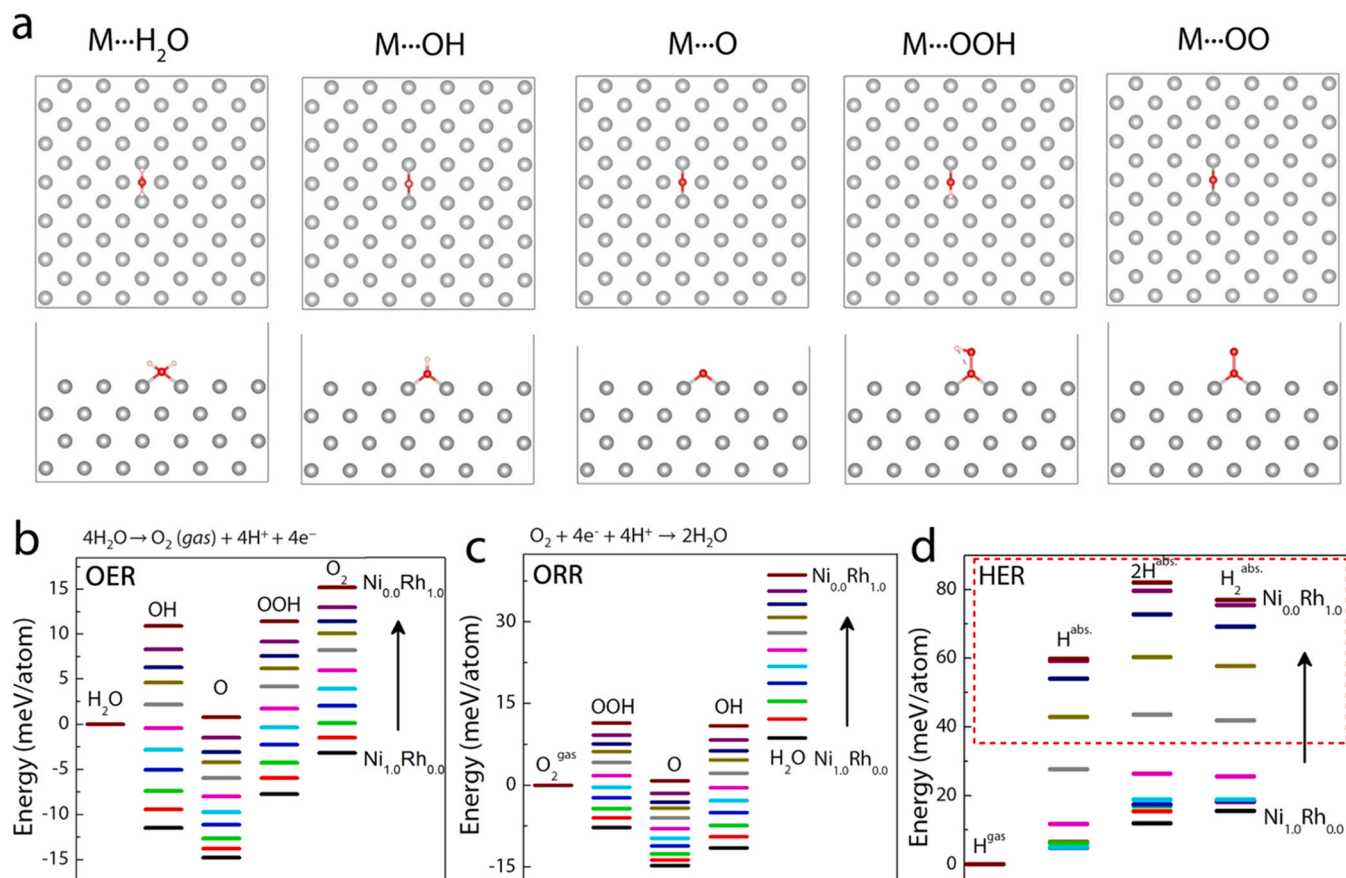


Fig. 5. a) Atomic structures of the RhNi (denoted here M) for various ORR and OER intermediates including H_2O , OH, O, OOH and OO using DFT calculation. The calculated absorption energy (E) in b) OER, c) ORR and d) HER are shown as function of the difference Rh-content in RhNi ranging from $x = 0.0$ to $x = 1.0$.

absorption energies (termed also as formation energies) were obtained under various Rh-content conditions for each electrochemical reaction step, as depicted in Figs. 5b and 5c. In both ORR and OER processes, the absorption energies for H₂O and O₂ exhibited a relatively higher values compared to other processes under a gradual increase with the Rh-content. This trend suggested that H₂O and O₂ are readily dissociated on the Ni_{1-x}Rh_x alloy surface with an increased Rh-content. Moreover, during the ORR and OER processes, the formation energy for the M-O step was relatively lower, which was attributed to the strong interaction between a single O atom and the metal surface compared to M-OH and M-OOH interactions, wherein stronger metal-O species interactions occur. Therefore, one can speculate that the M-O step in ORR and OER would be considered as a “rate-determining step”.

The calculated formation energies for proton adsorption, reduction, hydrogen intermediate formation, and H₂ desorption steps relative to the hydrogen evolution reaction (HER) revealed positive values across all stages in Rh_xNi_{1-x} alloy (Fig. 5d). These findings suggested that the entire series of HER processes in Rh_xNi_{1-x} alloy is less energetically unfavorable compared to oxygen reduction reaction (ORR) and oxygen evolution reaction (OER) steps. This phenomenon was attributed to the relatively stronger electronegativity of hydrogen compared to that of RhNi metals, implying a tendency for the metal to donate electrons to hydrogen. As the Rh content increased in Rh_xNi_{1-x} alloy, hydrogen dissociation from the metal surface become more facile due to enhanced electron donation from the metal. Interestingly, the predicted formation energies for all processes gradually increased until $x \sim 0.5$ in Ni_{1-x}Rh_x, beyond which they increased rapidly, indicating a much further difficulty in absorption on the surface beyond this point. Consequently, considering that RhNi with $x = 0.5$ (Rh-content) exhibited the strongest electric polarization, as evidenced by the previous DFT calculations above, it was reasonable to conclude that the enhanced electrocatalytic efficiency in RhNi can be achieved through the high electric polarization at the optimized Rh-content condition of approximately $x = 0.5$ within Rh_xNi_{1-x}.

3.7. Zn-air batteries applications with FeV₃O₈@RhNi as an air cathode

The practical feasibility of the FeV₃O₈@RhNi catalyst ORR/OER performance was tested by incorporating it as an air-electrode in a metal-air battery. We assembled a Zn-air secondary battery using a FeV₃O₈@RhNi-embedded porous gas diffusion layer (GDL) as the air cathode and a polished Zn plate as the anode. The photographic image of the Zn-air battery assembly is shown in Fig. 6a. For comparison, air cathodes were prepared under the same conditions by embedding electrodes with FeV₃O₈ and commercial noble metal RuO₂ + Pt/C catalysts. The Zn-air battery with the FeV₃O₈@RhNi air cathode exhibited a higher and more stable OCP (1.48 V for 24 h) than that with the FeV₃O₈ air cathode (1.31 V for 14 h) (Fig. S35). Fig. 6b displays the discharge polarization curves and the corresponding power density plots of the assembled Zn-air batteries. The peak power density of the Zn-air battery with the FeV₃O₈@RhNi air cathode was 186 mW cm⁻² at 320 mA cm⁻², which was higher than those of FeV₃O₈ (98 mW cm⁻² at 190 mA cm⁻²) and RuO₂ + Pt/C (120 mW cm⁻² at 240 mA cm⁻²). The voltage platform of the FeV₃O₈@RhNi cathode was 1.21 V at 10 mA cm⁻², which was higher than those of the RuO₂ + Pt/C (1.18 V) and FeV₃O₈ (1.16 V) electrodes (Fig. 6c). The Zn-air battery with the FeV₃O₈@RhNi air cathode achieved specific capacity of 810 mAh g⁻¹ at discharge current density of 10 mA cm⁻², (after adjusting to the weight of the dissipative Zn plate) and a high specific energy of 980 Wh g⁻¹. Additionally, the FeV₃O₈@RhNi air cathode demonstrates high specific capacities of 765, and 680 mA g⁻¹ at current densities of 20, and 50 mA cm⁻². These values were substantially greater than that of the RuO₂ + Pt/C-catalyzed air cathode (630 mA h g⁻¹) and FeV₃O₈ air cathode (541 mA h g⁻¹) at a current density of 10 mA cm⁻². The galvanostatic discharge step down-set up response of the FeV₃O₈@RhNi air-cathode battery was also examined at different current densities of

5–100 mA cm⁻² over 15 min. The FeV₃O₈@RhNi air cathode exhibited a small voltage drop when the current density rose from OCV to 100 mA cm⁻², and the voltage curve recovered when the current density fell from 100 mA cm⁻² to OCV, signifying its excellent rate capability and reversibility (Fig. 6d). The cycling stability of the Zn-air batteries was also examined using galvanostatic 10 min discharging/10 min charging at a current density of 10 mA cm⁻² (Fig. 6e and Fig. S36). The Zn-air battery with the FeV₃O₈@RhNi air cathode was cycled continuously (discharge (1.23 V)/charge (2.02 V) cycles) for 859 h (narrow voltage gap of 0.79 V) without obvious voltage fading and structural distortion (SEM images Fig. S37). In contrast, a rapid deterioration was observed for the RuO₂ + Pt/C and FeV₃O₈ air cathodes after 118 h (voltage gap of 0.99 V) and 248 h (voltage gap of 1.05 V), respectively. To reveal the reversibility of the battery process, the coulombic efficiency was obtained. When cycled at fixed current density of 10 mA cm⁻², the Zn-air battery based on the FeV₃O₈@RhNi air cathode provides a maximum average coulombic efficiency of 99.65% at a fixed capacity of 1 mAh cm⁻² (Fig. S38). This demonstrates the high ORR/OER performance of the FeV₃O₈@RhNi catalyst.

To further confirm whether the FeV₃O₈@RhNi catalyst can be used as an efficient air cathode for flexible battery device applications, a solid-state Zn-air battery was fabricated with a FeV₃O₈@RhNi catalyst-coated carbon cloth, polished Zn foil, and PVA-KOH-based gel used as the air cathode, anode, and electrolyte, respectively. The flexible Zn-air battery with the FeV₃O₈@RhNi catalyst delivered stable OCP for 10 h (Fig. S39). The discharge and charge cycles of the flexible Zn-air battery under various bending conditions are shown in Fig. 6f. During the 6h continuous discharge/charge cycles, the tiny voltage gap of the battery remained nearly constant at all bending angles. After continuous cycling, the flexible Zn-air battery provided sufficient power to the electrical fan under different bending conditions (Fig. 6f, inset).

A pouch Zn-air battery with FeV₃O₈@RhNi was also tested with a 6 M KOH/0.2 M ZnCl₄H₆O₄ solution as the electrolyte. Two pouch Zn-air batteries connected in series exhibited a higher OCP of 2.88 V (Fig. S39). The pouch Zn-air battery with the FeV₃O₈@RhNi catalyst showed a peak power density of 162 mW cm⁻² at 284 mA cm⁻² and a specific capacity of 738 mAh g⁻¹ at 5 mA cm⁻² (Figs S40 and S41). The long-term stability of the pouch Zn-air battery was then assessed via discharge/charge cycling at 10 mA cm⁻². The pouch Zn-air battery with the FeV₃O₈@RhNi catalyst was cycled (with a voltage gap of 0.96 V) for 198 h without obvious voltage fading, demonstrating excellent stability (Fig. 6g, schematic diagram of the pouch Zn-air battery Fig. 6h). Then, as a practical demonstration, the pouch Zn-air battery with FeV₃O₈@RhNi successfully powered an electric fan for several hours (Fig. 6i). Moreover, the two series-connected pouch Zn-air batteries with an OCP of 2.873 V generated sufficient power to operate an electric fan and yellow light-emitting diode (LED) simultaneously for several hours (Figs. 6j and 6k).

3.8. In situ synchrotron-based transmission-mode X-ray diffraction analysis

The improved stability of the Zn-air battery must be related to the excellent electrocatalytic activity of FeV₃O₈@RhNi during the electrochemical reaction. To directly monitor the progress of the electrochemical reaction in the Zn-air battery, *in situ* X-ray diffraction (XRD) analysis of the corresponding Zn-air batteries with FeV₃O₈ or FeV₃O₈@RhNi was conducted in discharge and charge modes for 10 min, which continue 6 h for each mode under room temperature (25 °C) and 1 atm condition (Figs. 7a, 7b and Figs. S42–47). Figs. 7c and 7d present the 2D XRD patterns and extracted one-dimensional (1D) XRD profiles of the (002), (010), and (011) planes of the Zn electrode for Zn-air batteries with FeV₃O₈ and FeV₃O₈@RhNi. For FeV₃O₈, a continuous increase in the XRD peak intensity of the (002), (010), and (011) planes was observed during the discharge or charge mode. This result suggested an irreversible electrochemical reaction in which the Zn

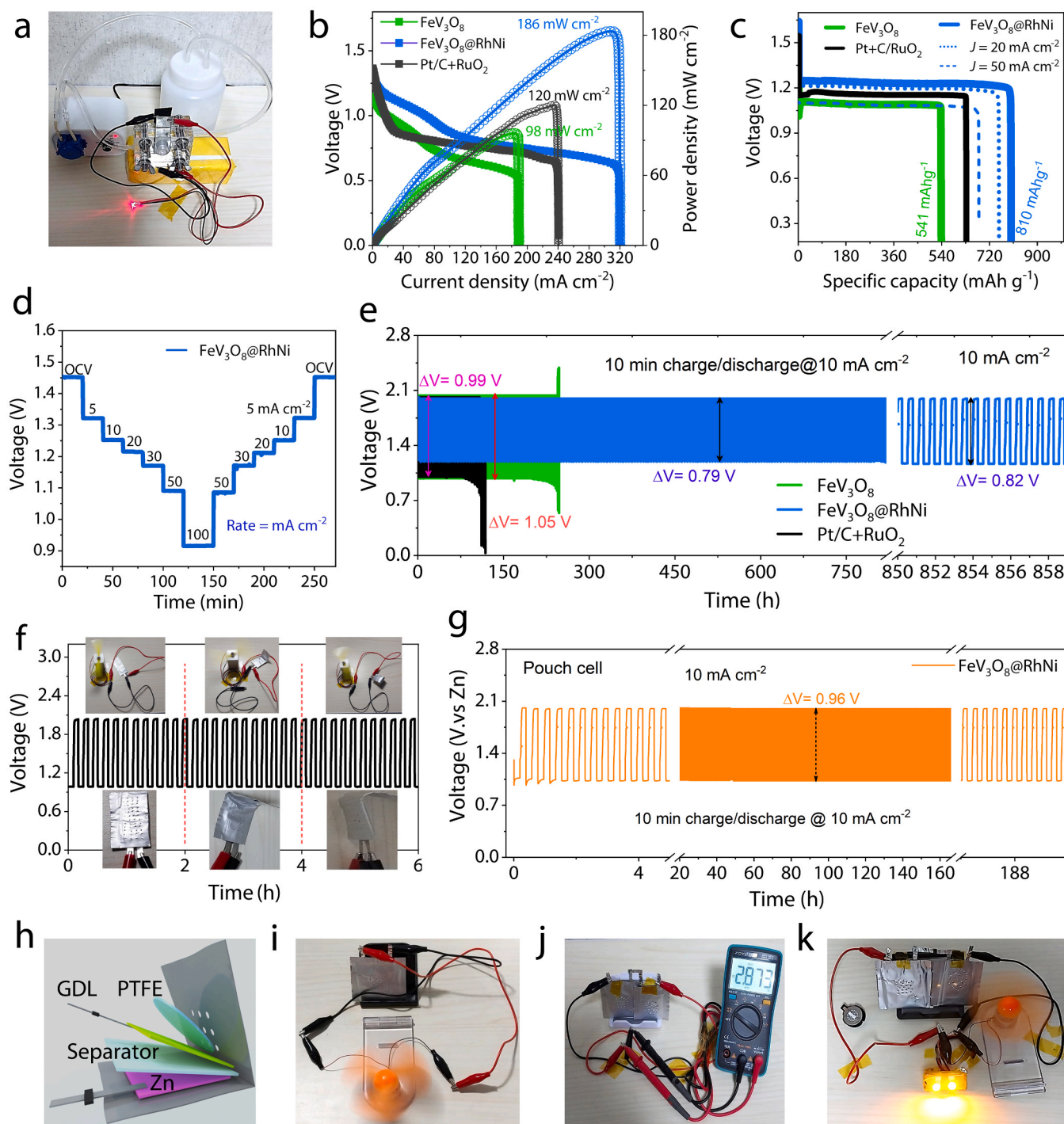


Fig. 6. Zn-air battery performances of electrocatalysts. a) Photographic image of the Zn-air battery measurement set-up powered by a $\text{FeV}_3\text{O}_8/\text{RhNi}$ air cathode. b) Steady-state polarization and power density curves of Zn-air batteries using $\text{RuO}_2 + \text{Pt/C}$, FeV_3O_8 , and $\text{FeV}_3\text{O}_8/\text{RhNi}$ catalysts as air cathodes. c) Discharge specific capacities of Zn-air batteries with $\text{RuO}_2 + \text{Pt/C}$, FeV_3O_8 , and $\text{FeV}_3\text{O}_8/\text{RhNi}$ air cathodes at a current density of 10 mA cm^{-2} . The mass of the Zn consumed was used to normalize the catalysts. The dashed lines associated with the $\text{FeV}_3\text{O}_8/\text{RhNi}$ air-cathode discharge at current densities of 20 and 50 mA cm^{-2} . d) Discharge curves of Zn-air battery using the $\text{FeV}_3\text{O}_8/\text{RhNi}$ catalyst as the air cathode at various current densities (5–100 mA cm^{-2}). e) Discharge/charge cycling response of Zn-air batteries using the $\text{RuO}_2 + \text{Pt/C}$, FeV_3O_8 , and $\text{FeV}_3\text{O}_8/\text{RhNi}$ air cathodes at a current density of 10 mA cm^{-2} . f) Flexible solid-state Zn-air battery cycling performance using the $\text{FeV}_3\text{O}_8/\text{RhNi}$ catalyst as the air cathode. Insets in the figures show the photographic images of the solid-state Zn-air battery performance at different states (flat, bent and twisted). g) Discharge/charge cycling response of a pouch Zn-air battery with the $\text{FeV}_3\text{O}_8/\text{RhNi}$ air cathode at a current density of 10 mA cm^{-2} . h) Schematic diagram of a pouch Zn-air battery assembly using the $\text{FeV}_3\text{O}_8/\text{RhNi}$ catalyst as the air cathode. i) Photographic image showing a fan powered by the single pouch Zn-air battery using the $\text{FeV}_3\text{O}_8/\text{RhNi}$ catalyst as the air cathode. j) OCP of two pouch Zn-air batteries connected in series. k) Photographic image of a fan and lit LED powered by two pouch Zn-air batteries connected in series using the $\text{FeV}_3\text{O}_8/\text{RhNi}$ catalyst as the air cathode.

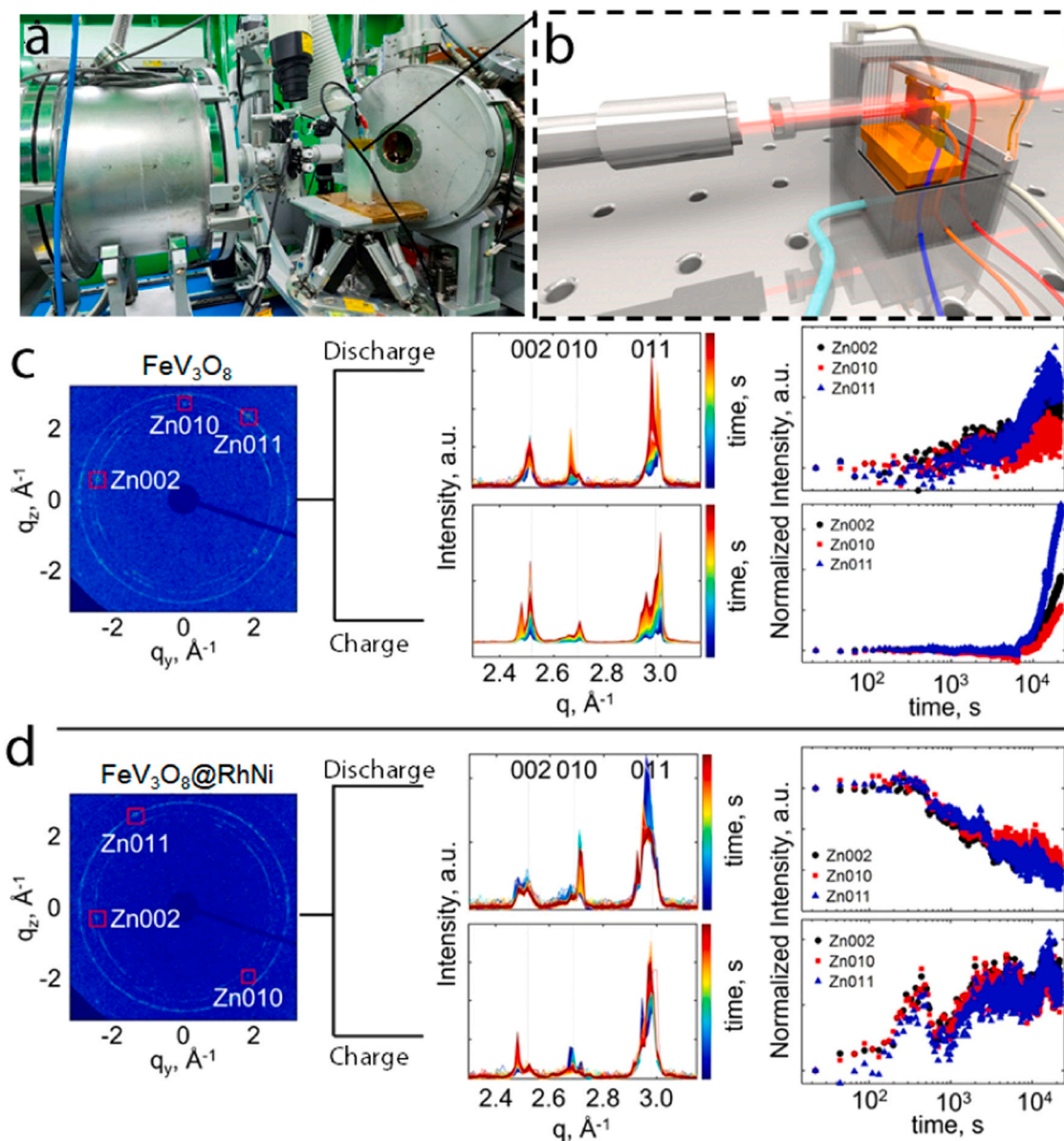
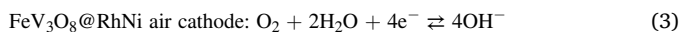


Fig. 7. *In situ* transmission-mode XRD analysis of the Zn-air battery with the FeV₃O₈/RhNi electrocatalyst. a) Experimental set-up for *in situ* transmission-mode XRD. b) Schematic image of the incident direction of the X-ray beam through the Zn-air battery during the device operation. c and d) 2D XRD patterns and the corresponding 1D radial averaged XRD profile on the (002), (010), and (011) planes of the Zn electrode for the Zn-air batteries with FeV₃O₈ and FeV₃O₈/RhNi, respectively, during the charge and discharge modes for 6 h each. The normalized intensity indicates the increase or decrease in the area intensity of the (002), (010), and (011) planes of the Zn electrode during the charge and discharge modes.

electrode in the Zn-air battery with FeV₃O₈ was continuously oxidized to emit abundant Zn²⁺ ions and thus accelerated the formation of ZnO regardless of the charge or discharge mode. In contrast, however, the Zn-air battery with FeV₃O₈/RhNi showed an increase or decrease in the XRD peaks of the (002), (010), and (011) planes of Zn, indicating a reversible electrochemical reaction in which the Zn electrode can be readily reduced and oxidized during the discharge and charge modes because of the distinctive electrocatalytic activity of FeV₃O₈/RhNi. Hence, the discharging (ORR) and the charging (OER) redox reactions of the Zn-air batteries can be expressed as [110–113]:



In Eqs. (1–4), the forward arrows mention the ORR processes, and the backward arrows indicate the OER processes. Notably, the Zn-air battery with FeV₃O₈/RhNi exhibited a consistent increasing and decreasing rate of peak intensity for the (002), (010), and (011) planes during the charge and discharge modes as compared to that of FeV₃O₈, suggesting that FeV₃O₈/RhNi effectively reduces the activation energy for the transformation mechanism between Zn and ZnO. These results demonstrate that FeV₃O₈/RhNi is a promising ORR/OER catalyst that can achieve high efficiency in metal-air battery applications.

4. Conclusions

Using the sequential hydrothermal process, we derived a new type of SAAE where the RhNi SAA homogeneously integrated on top of a

FeV₃O₈ electrocatalyst support. The $\Delta\phi$ between Rh and Ni increased the electric polarization of RhNi, which established a polarization-enhanced ohmic contact with FeV₃O₈ to facilitate efficient intermolecular charge transfer for efficient ORR and OER/HER. The FeV₃O₈@RhNi catalyst exhibited a high half-wave potential (0.90 V) for the ORR and required overpotentials of 120 and 200 mV to reach current densities of 10 and 100 mA cm⁻², respectively, for the OER. The electrochemical measurement of the HER demonstrated that the FeV₃O₈@RhNi catalyst displayed exceptional activity, achieving current densities of 10 and 100 mA cm⁻² at 8 and 41 mV, respectively. Moreover, the FeV₃O₈@RhNi alkaline electrolyzer demonstrated efficient generation of O₂/H₂ with an overall water splitting current density of 10 mA cm⁻² at 1.44 V. The rechargeable Zn–air batteries based on the FeV₃O₈@RhNi catalyst as an air cathode exhibited an OCP of 1.48 V, a specific capacity of 810 mAh g⁻¹, and a peak power density of 186 mW cm⁻² at 320 mA cm⁻², as well as excellent stability of >859 h at 10 mA cm⁻². In addition, the Zn–air pouch rechargeable battery using the FeV₃O₈@RhNi air cathode showed good stability for >196 h. The solid-state and pouch battery performances suggest that the FeV₃O₈@RhNi catalyst can be used to realize potential applications for flexible Zn–air batteries.

CRedit authorship contribution statement

C.B. conceived and designed the research idea, prepared the samples and conducted experiments and electrochemical analysis, wrote the manuscript & review. C.L. performed the density functional calculations. Y.-R.J. and K.H.C. helped to perform the TEM and NEXAFS measurements, respectively. C.B., Y.Y.K., and S.K. performed in-situ synchrotron-based XRD measurements and analysis. K.C. helped to perform the experiments. Y.P. and J.H.S. equipment provision and discussions. S.K. conceived and designed the research idea, supervised the research work, edited the manuscript. All of the authors discussed the data and commented on the manuscript.

Declaration of Competing Interest

The authors declare that they have no known competing financial interests or personal relationships that could have appeared to influence the work reported in this paper.

Data Availability

Data will be made available on request.

Acknowledgements

This work was supported by the Korea Institute of Energy Technology Evaluation and Planning (KETEP) and the Ministry of Trade, Industry & Energy (MOTIE) of the Republic of Korea (No. 2022400000020). This work was also supported by the National Research Foundation of Korea (NRF) funded by the Ministry of Science and ICT (No. 2022M3H4A1A04074153). J.H.S. was supported by the National Research Foundation of Korea (NRF) funded by Korean government (2022M3C1A3091988).

Appendix A. Supporting information

Supplementary data associated with this article can be found in the online version at [doi:10.1016/j.apcatb.2024.124072](https://doi.org/10.1016/j.apcatb.2024.124072).

References

- [1] J.M. Kim, A. Jo, K.A. Lee, H.J. Han, Y.J. Kim, H.Y. Kim, G.R. Lee, M. Kim, Y. Park, Y.S. Kang, Conformation-modulated three-dimensional electrocatalysts for high-performance fuel cell electrodes, *Sci. Adv.* 7 (2021) eabe9083, <https://doi.org/10.1126/sciadv.abe9083>.
- [2] Z. Yan, J.L. Hitt, J.A. Turner, T.E. Mallouk, Renewable electricity storage using electrolysis, *Proc. Natl. Acad. Sci. U. S. A.* 117 (2020) 12558–12563, <https://doi.org/10.1073/pnas.1821686116>.
- [3] S. Iqbal, B. Safdar, I. Hussain, K. Zhang, C. Chatzichristodoulou, Trends and Prospects of Bulk and Single-Atom Catalysts for the Oxygen Evolution Reaction, *Adv. Energy Mater.* 13 (2023) 2203913, <https://doi.org/10.1002/aenm.202203913>.
- [4] Y. Song, H. Kim, J.H. Jang, W. Bai, C. Ye, J. Gu, Y. Bu, Pt₃Ni Alloy Nanoparticle Electro-Catalysts with Unique Core-Shell Structure on Oxygen-Deficient Layered Perovskite for Solid Oxide Cells, *Adv. Energy Mater.* 13 (2023) 2302384, <https://doi.org/10.1002/aenm.202302384>.
- [5] M. Li, K. Duanmu, C. Wan, T. Cheng, L. Zhang, S. Dai, W. Chen, Z. Zhao, P. Li, H. Fei, Single-atom tailoring of platinum nanocatalysts for high-performance multifunctional electrocatalysis, *Nat. Catal.* 2 (2019) 495–503, <https://doi.org/10.1038/s41929-019-0279-6>.
- [6] C. Lin, J.-L. Li, X. Li, S. Yang, W. Luo, Y. Zhang, S.-H. Kim, D.-H. Kim, S.S. Shinde, Y.-F. Li, In-situ reconstructed Ru atom array on α -MnO₂ with enhanced performance for acidic water oxidation, *Nat. Catal.* 4 (2021) 1012–1023, <https://doi.org/10.1038/s41929-021-00703-0>.
- [7] D.K. Sarfo, J. Crawford, J.D. Riches, A.P. O'Mullane, Confining the electrodeposition of FeCoNi oxide within a Nafion layer for the fabrication of stable oxygen evolution electrocatalysts, *Chem. Catal.* 3 (2023) 100750, <https://doi.org/10.1016/j.checat.2023.100750>.
- [8] Z. Pei, H. Zhang, Z.-P. Wu, X.F. Lu, D. Luan, X.W. Lou, Atomically dispersed Ni activates adjacent Ce sites for enhanced electrocatalytic oxygen evolution activity, *Sci. Adv.* 9 (2023) eadh1320, <https://doi.org/10.1126/sciadv.adh1320>.
- [9] Y. Wang, Q. Lu, F. Li, D. Guan, Y. Bu, Atomic-Scale Configuration Enables Fast Hydrogen Migration for Electrocatalysis of Acidic Hydrogen Evolution, *Adv. Funct. Mater.* 33 (2023) 2213523, <https://doi.org/10.1002/adfm.202213523>.
- [10] L. Han, H. Cheng, W. Liu, H. Li, P. Ou, R. Lin, H.-T. Wang, C.W. Pao, A.R. Head, C.-H. Wang, A single-atom library for guided monometallic and concentration-complex multimetallic designs, *Nat. Mater.* 21 (2022) 681–688, <https://doi.org/10.1038/s41563-022-01252-y>.
- [11] Y. Da, R. Jiang, Z. Tian, X. Han, W. Chen, W. Hu, The applications of single-atom alloys in electrocatalysis: progress and challenges, *SmartMat* 4 (2023) e1136, <https://doi.org/10.1002/smm2.1136>.
- [12] M. Du, X. Li, H. Pang, Q. Xu, Alloy electrocatalysts, *EnergyChem* 5 (2023) 100083, <https://doi.org/10.1016/j.enchem.2022.100083>.
- [13] N. Cheng, L. Zhang, K. Doyle-Davis, X. Sun, Single-atom catalysts: from design to application, *Electrochem. Energy Rev.* 2 (2019) 539–573, <https://doi.org/10.1007/s41918-019-00050-6>.
- [14] X. Li, L. Liu, X. Ren, J. Gao, Y. Huang, B. Liu, Microenvironment modulation of single-atom catalysts and their roles in electrochemical energy conversion, *Sci. Adv.* 6 (2020) eabb6833, <https://doi.org/10.1126/sciadv.abb6833>.
- [15] Fang Luo, Shuyuan Pan, Yuhua Xie, Chen Li, Yingjie Yu, Zehui Yang, Atomically dispersed Ni electrocatalyst for superior urea-assisted water splitting, *J. Energy Chem.* 90 (2024) 1–6, <https://doi.org/10.1016/j.jechem.2023.10.007>.
- [16] Fang Luo, Shuyuan Pan, Yuhua Xie, Chen Li, Yingjie Yu, Haifeng Bao, Zehui Yang, Hydrazine-Assisted Acidic Water Splitting Driven by Iridium Single Atoms, *Adv. Sci.* 10 (2023) 2305058, <https://doi.org/10.1002/advs.202305058>.
- [17] Y. Chen, S. Ji, C. Chen, Q. Peng, D. Wang, Y. Li, Single-atom catalysts: synthetic strategies and electrochemical applications, *Joule* 2 (2018) 1242–1264, <https://doi.org/10.1016/j.joule.2018.06.019>.
- [18] J. Jones, H. Xiong, A.T. DeLaRiva, E.J. Peterson, H. Pham, S.R. Challa, G. Qi, S. Oh, M.H. Wiebenga, X.I. Pereira Hernández, Thermally stable single-atom platinum-on-ceria catalysts via atom trapping, *Science* 353 (2016) 150–154, <https://doi.org/10.1126/science.aaf8800>.
- [19] P. Liu, Y. Zhao, R. Qin, S. Mo, G. Chen, L. Gu, D.M. Chevrier, P. Zhang, Q. Guo, D. Zang, Photochemical route for synthesizing atomically dispersed palladium catalysts, *Science* 352 (2016) 797–800, <https://doi.org/10.1126/science.aaf5251>.
- [20] H. Wu, H. Li, X. Zhao, Q. Liu, J. Wang, J. Xiao, S. Xie, R. Si, F. Yang, S. Miao, Highly doped and exposed Cu (I)–N active sites within graphene towards efficient oxygen reduction for zinc–air batteries, *Energy Environ. Sci.* 9 (2016) 3736–3745, <https://doi.org/10.1039/C6EE01867J>.
- [21] J. Shan, C. Ye, Y. Jiang, M. Jaroniec, Y. Zheng, S.-Z. Qiao, Metal-metal interactions in correlated single-atom catalysts, *Sci. Adv.* 8 (2022) 1–14, <https://doi.org/10.1126/sciadv.abo0762>.
- [22] J. Shan, M. Li, L.F. Allard, S. Lee, M. Flytzani-Stephanopoulos, Mild oxidation of methane to methanol or acetic acid on supported isolated rhodium catalysts, *Nature* 551 (2017) 605–608, <https://doi.org/10.1038/nature24640>.
- [23] H. Shang, X. Zhou, J. Dong, A. Li, X. Zhao, Q. Liu, Y. Lin, J. Pei, Z. Li, Z. Jiang, Engineering unsymmetrically coordinated Cu–S₁N₃ single atom sites with enhanced oxygen reduction activity, *Nat. Commun.* 11 (2020) 3049, <https://doi.org/10.1038/s41467-020-16848-8>.
- [24] A. Kumar, X. Liu, J. Lee, B. Debnath, A.R. Jadhav, X. Shao, V.Q. Bui, Y. Hwang, Y. Liu, M.G. Kim, Discovering ultrahigh loading of single-metal-atoms via surface tensile-strain for unprecedented urea electrolysis, *Energy Environ. Sci.* 14 (2021) 6494–6505, <https://doi.org/10.1039/D1EE02603H>.
- [25] J. Lee, A. Kumar, M.G. Kim, T. Yang, X. Shao, X. Liu, Y. Liu, Y. Hong, A.R. Jadhav, M. Liang, Single-metal-atom dopants increase the Lewis acidity of metal oxides and promote nitrogen fixation, *ACS Energy Lett.* 6 (2021) 4299–4308, <https://doi.org/10.1021/acsenenergylett.1c02136>.
- [26] H. Yan, H. Cheng, H. Yi, Y. Lin, T. Yao, C. Wang, J. Li, S. Wei, J. Lu, Single-atom Pd1/graphene catalyst achieved by atomic layer deposition: remarkable

- performance in selective hydrogenation of 1, 3-butadiene, *J. Am. Chem. Soc.* 137 (2015) 10484–10487, <https://doi.org/10.1021/jacs.5b0648>.
- [27] E. Zhang, A. Dong, K. Yin, C. Ye, Y. Zhou, C. Tan, M. Li, X. Zheng, Y. Wang, X. Gao, H. Li, D. Wang, S. Guo, Electron Localization in Rationally Designed PtPd Single-Atom Alloy Catalyst Enables High-Performance Li–O₂ Batteries, *J. Am. Chem. Soc.* 146 (2024) 2339–2344, <https://doi.org/10.1021/jacs.3c12734>.
- [28] X.F. Yang, A. Wang, B. Qiao, J. Li, J. Liu, T. Zhang, Single-Atom Catalysts: A New Frontier in Heterogeneous Catalysis, *Acc. Chem. Res.* 46 (2013) 1740–1748, <https://doi.org/10.1021/ar300361m>.
- [29] Y. Chen, S. Ji, C. Chen, Q. Peng, D. Wang, Y. Li, "Single-Atom Catalysts: Synthetic Strategies and Electrochemical Applications", *Joule* 2 (2018) 1242–1264, <https://doi.org/10.1016/j.joule.2018.06.019>.
- [30] J. Li, C. Chen, L. Xu, Y. Zhang, W. Wei, E. Zhao, Y. Wu, C. Chen, Challenges and Perspectives of Single-Atom-Based Catalysts for Electrochemical Reactions, *JACS Au* 3 (2023) 736–755, <https://doi.org/10.1021/jacsau.3c00001>.
- [31] Y. Cao, S. Chen, Q. Luo, H. Yan, Y. Lin, W. Liu, L. Cao, J. Lu, J. Yang, T. Yao, Atomic-level insight into optimizing the hydrogen evolution pathway over a Co₁-N₄ single-site photocatalyst, *Angew. Chem. Int. Ed. Engl.* 56 (2017) 12191–12196, <https://doi.org/10.1002/ange.201706467>.
- [32] K. Chen, Q. Zhong, W. Chen, B. Sang, Y. Wang, T. Yang, Y. Liu, Y. Zhang, H. Zhang, Short-Chain Ligand-Passivated Stable α -CsPbI₃ Quantum Dot for All-Inorganic Perovskite Solar Cells, *Adv. Funct. Mater.* 29 (2019) 1900991, <https://doi.org/10.1002/adfm.201900991>.
- [33] J. Wang, J. Li, Y. Zhou, C. Yu, Y. Hua, Y. Yu, R. Li, X. Lin, R. Chen, H. Wu, H. Xia, H.L. Wang, Tuning an Electrode Work Function Using Organometallic Complexes in Inverted Perovskite Solar Cells, *J. Am. Chem. Soc.* 143 (2021) 7759–7768, <https://doi.org/10.1021/jacs.1c02118>.
- [34] N. Zou, X. Zhou, G. Chen, N.M. Andoy, W. Jung, G. Liu, P. Chen, Cooperative communication within and between single nanocatalysts, *Nat. Chem.* 10 (2018) 607–614, <https://doi.org/10.1038/s41557-018-0022-y>.
- [35] L. Tao, Y. Wang, Y. Zou, N. Zhang, Y. Zhang, Y. Wu, Y. Wang, R. Chen, S. Wang, Charge transfer modulated activity of carbon-based electrocatalysts, *Adv. Energy Mater.* 10 (2020) 1901227, <https://doi.org/10.1038/s41557-018-0022-y>.
- [36] J. Zhang, B. Che, W. Zhao, Y. Fang, R. Han, Y. Yang, J. Liu, T. Yang, T. Chen, N. Yuan, J. Ding, S. Liu, Polar Species for Effective Dielectric Regulation to Achieve High-Performance CsPbI₃ Solar Cells, *Adv. Mater.* 34 (2022) 2202735, <https://doi.org/10.1002/adma.202202735>.
- [37] S. Ji, Y. Chen, X. Wang, Z. Zhang, D. Wang, Y. Li, Chemical synthesis of single atomic site catalysts, *Chem. Rev.* 120 (2020) 11900–11955, <https://doi.org/10.1021/acs.chemrev.9b00818>.
- [38] J. Li, C. Chen, L. Xu, Y. Zhang, W. Wei, E. Zhao, Y. Wu, C. Chen, Challenges and Perspectives of Single-Atom-Based Catalysts for Electrochemical Reactions, *JACS Au* 3 (2023) 736–755, <https://doi.org/10.1021/jacsau.3c00001>.
- [39] M.K. Christensen, J.K. Mathiesen, S.B. Simonsen, P. Norby, Transformation and migration in secondary zinc-air batteries studied by in situ synchrotron X-ray diffraction and X-ray tomography, *J. Mater. Chem. A* 7 (2019) 6459–6466, <https://doi.org/10.1039/C8TA11554K>.
- [40] F. Santos, J. Abad, M. Vila, G.R. Castro, A. Urbina, A.J.F. Romero, In situ synchrotron x-ray diffraction study of Zn/Bi₂O₃ electrodes prior to and during discharge of Zn-air batteries: Influence on ZnO deposition, *Electrochim. Acta* 281 (2018) 133–141, <https://doi.org/10.1016/j.electacta.2018.05.138>.
- [41] Y.J. Song, X. Sun, L.P. Ren, L. Zhao, F.P. Kong, J.J. Wang, "Synchrotron X-Rays Characterizations of Metal-Air Batteries", in: *J. Electrochem.*, 28, 2022 210846, <https://doi.org/10.13208/j.electrochem.210846>.
- [42] R. F. Lang, T. Arlt, I. Manke, J. Kowal, X-ray tomography as a powerful method for zinc-air battery research, *J. Power Sources* 370 (2017) 45–51, <https://doi.org/10.1016/j.jpowsour.2017.10.010>.
- [43] D. Schröder, T. Arlt, U. Krewer, I. Manke, Analyzing transport paths in the air electrode of a zinc air battery using X-ray tomography, *Electrochem. Commun.* 40 (2014) 88–91, <https://doi.org/10.1016/j.elecom.2014.01.001>.
- [44] A. Nakata, H. Arai, H. Murayama, K. Fukuda, T. Yamane, T. Hirai, Y. Uchimoto, J. Yamaki, Z. Ogumi, In situ Zn/ZnO mapping elucidating for "shape change" of zinc electrode, *APL Mater.* 6 (2018) 047703, <https://doi.org/10.1063/1.5011272>.
- [45] J. Yin, J. Wang, Y. Ma, J. Yu, J. Zhou, Z. Fan, Recent Advances in the Controlled Synthesis and Catalytic Applications of TwoDimensional Rhodium Nanomaterials, *ACS Mater. Lett.* 3 (2021) 121–133.
- [46] M.T. Chen, J.J. Duan, J.J. Feng, L.P. Mei, Y. Jiao, L. Zhang, A.J. Wang, Iron, rhodium-codoped Ni₂P nanosheets arrays supported on nickel foam as an efficient bifunctional electrocatalyst for overall water splitting, *J. Colloid Interface Sci.* 605 (2022) 888–896.
- [47] F. Luo, Y. Yu, X. Long, C. Li, T. Xiong, Z. Yang, Boosting catalytic activity toward methanol oxidation reaction for platinum via heterostructure engineering, *J. Colloid Interface Sci.* 656 (2024) 450–456, <https://doi.org/10.1016/j.jcis.2023.11.077>.
- [48] S. Pan, C. Li, T. Xiong, Y. Xie, F. Luo, Z. Yang, Hydrogen spillover in MoO_x/Rh hierarchical nanosheets boosts alkaline HER catalytic activity, *Appl. Catal. B: Environ.* 341 (2024) 123275.
- [49] R.T. Hannagan, G. Giannakakis, M.F. Stephanopoulos, E.C.H. Sykes, Single-atom alloy catalysis, *Chem. Rev.* 120 (2020) 12044–12088.
- [50] D.S. Tran, H. Park, H. Kim, S.K. Kim, Electrodeposited NiRh alloy as an efficient low-precious metal catalyst for alkaline hydrogen oxidation reaction, *Int. J. Energy Res.* 45 (2021) 5325–5336.
- [51] R. Wei, Z. Chen, H. Lv, X. Zheng, X. Ge, L. Sun, L. Sun, K. Song, C. Kong, W. Zhang, B. Liu, Ultrafine RhNi Nanocatalysts Confined in Hollow Mesoporous Carbons for a Highly Efficient Hydrogen Production from Ammonia Borane, *Inorg. Chem.* 60 (2021) 6820–6828.
- [52] N.Q. Tran, Bao T.N. Le, T.N.M. Le, L.T. Duy, T.B. Phan, Y. Hong, T.K. Truong, T.L. H. Doan, J. Yu, H. Lee, Coupling Amorphous Ni Hydroxide Nanoparticles with Single-Atom Rh on Cu Nanowire Arrays for Highly Efficient Alkaline Seawater Electrolysis, *J. Phys. Chem. Lett.* 13 (2022) 8192–8199.
- [53] G. Wu, X. Zheng, P. Cui, H. Jiang, X. Wang, Y. Qu, W. Chen, Y. Lin, H. Li, X. Han, Y. Hu, P. Liu, Q. Zhang, J. Ge, Y. Yao, R. Sun, Y. Wu, L. Gu, X. Hong, Y. Li, A general synthesis approach for amorphous noble metal nanosheets, *Nat. Commun.* 10 (2019) 4855.
- [54] Y. Chen, Z. Fan, Z. Zhang, W. Niu, C. Li, N. Yang, B. Chen, H. Zhang, Two-Dimensional Metal Nanomaterials: Synthesis, Properties, and Applications, *Chem. Rev.* 118 (2018) 6409–6455.
- [55] M. Yoo, Y.S. Yu, H. Ha, S. Lee, J.S. Choi, S. Oh, E. Kang, H. Choi, H. An, K.S. Lee, J.Y. Park, R. Celestre, M.A. Marcus, K. Nowrouzi, D. Taube, D.A. Shapiro, WooChul Jung, C. Kim, H.Y. Kim, A tailored oxide interface creates dense Pt single-atom catalysts with high catalytic activity, *Energy Environ. Sci.* 13 (2020) 1231–1239.
- [56] A. Pei, G. Li, L. Zhu, Z. Huang, J. Ye, Y.C. Chang, S.M. Osman, C.W. Pao, Q. Gao, B.H. Chen, R. Luque, Nickel Hydroxide-Supported Ru Single Atoms and Pd Nanoclusters for Enhanced Electrocatalytic Hydrogen Evolution and Ethanol Oxidation, *Adv. Funct. Mater.* 32 (2022) 2208587.
- [57] Y. Yuan, C. Zhang, B. Jia, F. Wei, X. Zhang, G. Wu, L. Li, F. Chen, J. Hao, P. Lu, Single rhodium atom embedded two dimensional MoSi₂N₄: A promising electrocatalyst for oxygen reduction reaction, *Appl. Surf. Sci.* 653 (2024) 159361.
- [58] H. Duan, N. Yan, R. Yu, C.R. Chang, G. Zhou, H.S. Hu, H. Rong, Z. Niu, J. Mao, H. Asakura, T. Tanaka, P.J. Dyson, J. Li, Y. Li, *Nat. Commun.* 5 (2014) 3093.
- [59] L. Zhao, C. Xu, H. Su, J. Liang, S. Lin, L. Gu, X. Wang, M. Chen, N. Zheng, Single-crystalline rhodium nanosheets with atomic thickness, *Adv. Sci.* 2 (2015) 1500100.
- [60] J. Zhu, M. Xiao, G. Li, S. Li, J. Zhang, G. Liu, L. Ma, T. Wu, J. Lu, A. Yu, D. Su, H. Jin, S. Wang, Z. Chen, A triphasic bifunctional oxygen electrocatalyst with tunable and synergetic interfacial structure for rechargeable Zn-air batteries, *Adv. Energy Mater.* (2019) 1903003.
- [61] Y. Pan, J. Wei, D. Han, Q. Xu, D. Gao, Y. Yang, Y. Wei, Hetero-nanostructures constructed by 2D porous metal oxide/hydroxide nanosheets supported on 1D hollow Co₃S₂ nanowires for hybrid super capacitors with high areal capacity, *Inorg., Chem. Front.* 8 (2021) 4676–4684.
- [62] L. Pan, A. Parnière, O. Dunseath, D. Fongalland, G. Nicolau, C.C. Weber, J. Lu, M. Klingenhof, A. Arincheif, H.S. Oh, P.Y. Blanchard, S. Cavaliere, M. Heggen, R. E.D. Borkowski, A.M. Bonastre, F. Dionigi, J. Sharman, D. Jones, P. Strasser, Enhancing the performance of shape-controlled octahedral rhodium-doped ptmi nanoalloys inside hydrogen-air fuel cell cathodes using a rational design of catalysts, supports, and layering, *ACS Catal.* 14 (2024) 10–20.
- [63] W. Zhang, X. Zhang, L. Chen, J. Dai, Y. Ding, L. Ji, J. Zhao, M. Yan, F. Yang, C. R. Chang, S. Guo, Single-walled carbon nanotube induced optimized electron polarization of rhodium nanocrystals to develop an interface catalyst for highly efficient electrocatalysis, *ACS Catal.* 8 (2018) 8092–8099.
- [64] J. Ban, X. Wen, H. Xu, Z. Wang, X. Liu, G. Cao, G. Shao, J. Hu, Dual Evolution in Defect and Morphology of Single-Atom Dispersed Carbon Based Oxygen Electrocatalyst, *Adv. Funct. Mater.* 31 (2021) 2010472.
- [65] X. Han, X. Ling, D. Yu, D. Xie, L. Li, S. Peng, C. Zhong, N. Zhao, Y. Deng, W. Hu, Atomically dispersed binary Co-Ni Sites in nitrogen-doped hollow carbon nanotubes for reversible oxygen reduction and evolution, *Adv. Mater.* (2019) 1905622.
- [66] Y. Wang, X. Ge, Q. Lu, W. Bai, C. Ye, Z. Shao, Y. Bu, Accelerated deprotonation with a hydroxysilicon alkali solid for rechargeable zinc-air batteries, *Nat. Commun.* 14 (2023) 6968, <https://doi.org/10.1038/s41467-023-42728-y>.
- [67] X.Q. Tan, S.F. Ng, A.R. Mohamed, W.J. Ong, Point-to-face contact heterojunctions: Interfacial design of OD nanomaterials on 2D g-C₃N₄ towards photocatalytic energy applications, *Carbon Energy* 4 (2022) 665–730, <https://doi.org/10.1002/cey2.252>.
- [68] R. Majee, A. Kumar, T. Das, S. Chakraborty, S. Bhattacharyya, Tweaking nickel with minimal silver in a heterogeneous alloy of decahedral geometry to deliver platinum-like hydrogen evolution activity, *Angew. Chem. Int. Ed. Engl.* 59 (2020) 2881–2889, <https://doi.org/10.1002/anie.201913704>.
- [69] J. Mao, C.-T. He, J. Pei, Y. Liu, J. Li, W. Chen, D. He, D. Wang, Y. Li, Isolated Ni atoms dispersed on Ru nanosheets: High-performance electrocatalysts toward hydrogen oxidation reaction, *Nano Lett.* 20 (2020) 3442–3448, <https://doi.org/10.1021/acs.nanolett.0c00364>.
- [70] H. Wang, L. Jiao, L. Zheng, Q. Fang, Y. Qin, X. Luo, X. Wei, L. Hu, W. Gu, J. Wen, PdBi single-atom alloy aerogels for efficient ethanol oxidation, *Adv. Funct. Mater.* 31 (2021) 2103465, <https://doi.org/10.1002/adfm.202103465>.
- [71] G. Ma, Q. Xue, J. Zhu, X. Zhang, X. Wang, H. Yao, G. Zhou, Y. Chen, Ultrafine Rh nanocrystals decorated ultrathin NiO nanosheets for urea electro-oxidation, *Appl. Catal. B: Environ.* 265 (2020) 118567, <https://doi.org/10.1016/j.apcatb.2019.118567>.
- [72] W. Wan, Y. Zhao, S. Wei, C.A. Triana, J. Li, A. Arcifa, C.S. Allen, R. Cao, G. R. Patzke, Mechanistic insight into the active centers of single/dual-atom Ni/Fe-based oxygen electrocatalysts, *Nat. Commun.* 12 (2021) 5589, <https://doi.org/10.1038/s41467-021-25811-0>.
- [73] C. Balamurugan, C. Lee, K. Cho, J. Kim, B. Park, W. Kim, N. Lim, H. Kim, Y. Pak, K.H. Chae, High-performance rechargeable metal-air batteries enabled by efficient charge transport in multielement random alloy electrocatalyst, *Appl. Catal. B: Environ.* 330 (2023) 122631, <https://doi.org/10.1016/j.apcatb.2023.122631>.

- [74] C.X. Zhao, J.N. Liu, J. Wang, C. Wang, X. Guo, X.-Y. Li, X. Chen, L. Song, B.-Q. Li, Q. Zhang, A clicking confinement strategy to fabricate transition metal single-atom sites for bifunctional oxygen electrocatalysis, *Sci. Adv.* 8 (2022) eabn5091, <https://doi.org/10.1126/sciadv.abn5091>.
- [75] W. Wan, C.A. Triana, J. Lan, J. Li, C.S. Allen, Y. Zhao, M. Iannuzzi, G.R. Patzke, Bifunctional single atom electrocatalysts: coordination–performance correlations and reaction pathways, *ACS Nano* 14 (2020) 13279–13293, <https://doi.org/10.1021/acsnano.0c05088>.
- [76] M. Zhao, H. Liu, H. Zhang, W. Chen, H. Sun, Z. Wang, B. Zhang, L. Song, Y. Yang, C. Ma, A pH-universal ORR catalyst with single-atom iron sites derived from a double-layer MOF for superior flexible quasi-solid-state rechargeable Zn–air batteries, *Energy Environ. Sci.* 14 (2021) 6455–6463, <https://doi.org/10.1039/D1EE01602D>.
- [77] M. Xiao, Z. Xing, Z. Jin, C. Liu, J. Ge, J. Zhu, Y. Wang, X. Zhao, Z. Chen, Preferentially engineering FeN₄ edge sites onto graphitic nanosheets for highly active and durable oxygen electrocatalysis in rechargeable Zn–air batteries, *Adv. Mater.* 32 (2020) 2004900, <https://doi.org/10.1002/adma.202004900>.
- [78] H. Jiang, J. Gu, X. Zheng, M. Liu, X. Qiu, L. Wang, W. Li, Z. Chen, X. Ji, J. Li, Defect-rich and ultrathin N doped carbon nanosheets as advanced trifunctional metal-free electrocatalysts for the ORR, OER and HER, *Energy Environ. Sci.* 12 (2019) 322–333, <https://doi.org/10.1039/C8EE03276A>.
- [79] G. Yang, J. Zhu, P. Yuan, Y. Hu, G. Qu, B.-A. Lu, X. Xue, H. Yin, W. Cheng, J. Cheng, Regulating Fe-spin state by atomically dispersed Mn-N in Fe-NC catalysts with high oxygen reduction activity, *Nat. Commun.* 12 (2021) 1734, <https://doi.org/10.1038/s41467-021-21919-5>.
- [80] Y. Sugawara, K. Kamata, A. Ishikawa, Y. Tateyama, T. Yamaguchi, Efficient oxygen evolution electrocatalysis on CaFe₂O₄ and its reaction mechanism, *ACS Appl. Energy Mater.* 4 (2021) 3057–3066, <https://doi.org/10.1021/acsaem.0c02710>.
- [81] C.T. Carver, B.D. Matson, J.M. Mayer, Electrocatalytic oxygen reduction by iron tetra-arylporphyrins bearing pendant proton relays, *J. Am. Chem. Soc.* 134 (2012) 5444–5447, <https://doi.org/10.1021/ja211987f>.
- [82] J. Guan, X. Wen, Q. Zhang, Z. Duan, Atomic rhodium catalysts for hydrogen evolution and oxygen reduction reactions, *Carbon* 164 (2020) 121–128, <https://doi.org/10.1016/j.carbon.2020.03.055>.
- [83] Y. Wang, R. Yang, Y. Ding, B. Zhang, H. Li, B. Bai, M. Li, Y. Cui, J. Xiao, Z.-S. Wu, Unraveling oxygen vacancy site mechanism of Rh doped RuO₂ catalyst for long-lasting acidic water oxidation, *Nat. Commun.* 14 (2023) 1412, <https://doi.org/10.1038/s41467-023-37008-8>.
- [84] S. Anantharaj, S. Kundu, Do the Evaluation Parameters Reflect Intrinsic Activity of Electrocatalysts in Electrochemical Water Splitting? *ACS Energy Lett.* 4 (2019) 1260–1264, <https://doi.org/10.1021/acsenerylett.9b00686>.
- [85] C. Madan, C.S. Tiwary, A. Halder, Enhancing the oxygen evolution activity of nitrogen-doped graphitic carbon shell- embedded nickel/nickel oxide nanoparticles by surface dissolution, *Mater. Chem. Front.* 4 (2020) 3267–3279, <https://doi.org/10.1039/D0QM00526F>.
- [86] X. Han, Y. Yu, Y. Huang, D. Liu, B. Zhang, Photogenerated carriers boost water splitting activity over transition-metal/semiconducting metal oxide bifunctional electrocatalysts, *ACS Catal.* 7 (2017) 6464–6470, <https://doi.org/10.1021/acscatal.7b01823>.
- [87] J. Weil, H. Tang, L. Sheng, R. Wang, M. Fan, J. Wan, Y. Wu, Z. Zhang, S. Zhou, J. Zeng, Site-specific metal-support interaction to switch the activity of Ir single atoms for oxygen evolution reaction, *Nat. Commun.* 15 (2024) 559, <https://doi.org/10.1038/s41467-024-44815-0>.
- [88] K.S. Joya, X. Salac, *In situ* Raman and surface-enhanced Raman spectroscopy on working electrodes: spectroelectrochemical characterization of water oxidation electrocatalysts, *Phys. Chem. Chem. Phys.* 17 (2015) 21094–21103, <https://doi.org/10.1039/C4CP05053C>.
- [89] X. Li, Y. Wang, J. Wang, Y. Da, J. Zhang, L. Li, C. Zhong, Y. Deng, X. Han, W. Hu, Sequential electrodeposition of bifunctional catalytically active structures in MoO₃/Ni–NiO composite electrocatalysts for selective hydrogen and oxygen evolution, *Adv. Mater.* 32 (2020) 2003414, <https://doi.org/10.1002/adma.202003414>.
- [90] X. Gao, H. Zhang, Q. Li, X. Yu, Z. Hong, X. Zhang, C. Liang, Z. Lin, Hierarchical NiCo₂O₄ hollow microcuboids as bifunctional electrocatalysts for overall water-splitting, *Angew. Chem. Int. Ed. Engl.* 55 (2016) 6290–6294, <https://doi.org/10.1002/anie.201600525>.
- [91] S.A. Vilekar, I. Fishtik, R. Datta, Kinetics of the Hydrogen Electrode Reaction, *J. Electrochem. Soc.* 157 (2010) B1040–B1050, <https://doi.org/10.1149/1.3385391>.
- [92] E. Skúlason, V. Tripkovic, M.E. Björketun, S. Gudmundsdóttir, G. Karlberg, J. Rossmeis, T. Bligaard, H. Jónsson, J.K. Nørskov, Modeling the electrochemical hydrogen oxidation and evolution reactions on the basis of density functional theory calculations, *J. Phys. Chem. C* 114 (2010) 18182–18197, <https://doi.org/10.1021/jp1048887>.
- [93] M. Gu, X. Deng, M. Lin, H. Wang, A. Gao, X. Huang, X. Zhang, Ultrathin NiCo bimetallic molybdate nanosheets coated CuO_x nanotubes: heterostructure and bimetallic synergistic optimization of the active site for highly efficient overall water splitting, *Adv. Energy Mater.* 11 (2021) 2102361, <https://doi.org/10.1002/aenm.202102361>.
- [94] N. Zhang, L. Li, J. Wang, Z. Hu, Q. Shao, X. Xiao, X. Huang, Surface-regulated rhodium–antimony nanorods for nitrogen fixation, *Angew. Chem. Int. Ed. Engl.* 132 (2020) 8143–8148, <https://doi.org/10.1002/anie.201915747>.
- [95] Y. Xiong, J. Dong, Z.-Q. Huang, P. Xin, W. Chen, Y. Wang, Z. Li, Z. Jin, W. Xing, Z. Zhuang, Single-atom Rh/N-doped carbon electrocatalyst for formic acid oxidation, *Nat. Nanotechnol.* 15 (2020) 390–397, <https://doi.org/10.1038/s41565-020-0665-x>.
- [96] W. Liu, H. Feng, Y. Yang, Y. Niu, L. Wang, P. Yin, S. Hong, B. Zhang, X. Zhang, M. Wei, Highly-efficient RuNi single-atom alloy catalysts toward chemoselective hydrogenation of nitroarenes, *Nat. Commun.* 13 (2022) 3188, <https://doi.org/10.1038/s41467-022-30536-9>.
- [97] P. Zhai, M. Xia, Y. Wu, G. Zhang, J. Gao, B. Zhang, S. Cao, Y. Zhang, Z. Li, Z. Fan, Engineering single-atomic ruthenium catalytic sites on defective nickel-iron layered double hydroxide for overall water splitting, *Nat. Commun.* 12 (2021) 4587, <https://doi.org/10.1038/s41467-021-24828-9>.
- [98] Q. Chang, Y. Hong, H.J. Lee, J.H. Lee, D. Ologunagba, Z. Liang, J. Kim, M.J. Kim, J.W. Hong, L. Song, Achieving complete electrooxidation of ethanol by single atomic Rh decoration of Pt nanocubes, *Proc. Natl. Acad. Sci. U. S. A.* 119 (2022) e2112109119, <https://doi.org/10.1073/pnas.2112109119>.
- [99] A. Kumar, V.Q. Bui, J. Lee, L. Wang, A.R. Jadhav, X. Liu, X. Shao, Y. Liu, J. Yu, Y. Hwang, Moving beyond bimetallic-alloy to single-atom dimer atomic-interface for all-pH hydrogen evolution, *Nat. Commun.* 12 (2021) 6766, <https://doi.org/10.1038/s41467-021-27145-3>.
- [100] Z. Lu, B. Wang, Y. Hu, W. Liu, Y. Zhao, R. Yang, Z. Li, J. Luo, B. Chi, Z. Jiang, An isolated zinc–cobalt atomic pair for highly active and durable oxygen reduction, *Angew. Chem. Int. Ed. Engl.* 131 (2019) 2648–2652, <https://doi.org/10.1002/anie.201810175>.
- [101] F. De Groot, M. Grioni, J.C. Fuggle, J. Ghijsen, G.A. Sawatzky, H. Petersen, Oxygen 1s x-ray-absorption edges of transition-metal oxides, *Phys. Rev. B* 40 (1989) 5715, <https://doi.org/10.1103/PhysRevB.40.5715>.
- [102] S. Kumar, S. Gautam, T. Song, K.H. Chae, K. Jang, S. Kim, Electronic structure study of Co doped CeO₂ nanoparticles using X-ray absorption fine structure spectroscopy, *J. Alloy. Compd.* 611 (2014) 329–334, <https://doi.org/10.1016/j.jallcom.2014.05.025>.
- [103] K. Kumari, R.N. Aljawfi, Y. Katharria, S. Dwivedi, K. Chae, R. Kumar, A. Alshoaibi, P. Alvi, S. Dalela, S. Kumar, Study the contribution of surface defects on the structural, electronic structural, magnetic, and photocatalyst properties of Fe: CeO₂ nanoparticles, *J. Electron. Spectrosc. Relat. Phenom.* 235 (2019) 29–39, <https://doi.org/10.1016/j.elspec.2019.06.004>.
- [104] S. Soni, M. Dave, B. Dalela, P. Alvi, S. Kumar, S. Sharma, D. Phase, M. Gupta, S. Dalela, Effect of defects and oxygen vacancies on the RTFM properties of pure and Gd-doped CeO₂ nanomaterials through soft XAS, *Appl. Phys. A* 126 (2020) 1–11, <https://doi.org/10.1007/s00339-020-03777-y>.
- [105] M. Ge, H. Wang, E. Liu, J. Liu, J. Jiang, Y. Li, Z. Xu, H. Li, On the origin of ferromagnetism in CeO₂ nanocubes, *Appl. Phys. Lett.* 93 (2008) 062505, <https://doi.org/10.1063/1.2972118>.
- [106] D.R. Ou, T. Mori, F. Ye, J. Zou, G. Auchterlonie, J. Drennan, Oxygen-vacancy ordering in lanthanide-doped ceria: dopant-type dependence and structure model, *Phys. Rev. B* 77 (2008) 024108, <https://doi.org/10.1103/PhysRevB.77.024108>.
- [107] Y. Guo, J. Sun, Y. Tang, X. Jia, Y. Nie, Z. Geng, C. Wang, J. Zhang, X. Tan, D. Zhong, Efficient Interfacial Electrons Transfer Induced by Hollow-Structured ZnIn₂S₄ Extending Hot Electrons Lifetimes, *Energy Environ. Sci.* 16 (2023) 3462–3473, <https://doi.org/10.1039/D3EE01522J>.
- [108] Y. Lian, W. Yang, C. Zhang, H. Sun, Z. Deng, W. Xu, L. Song, Z. Ouyang, Z. Wang, J. Guo, Unpaired 3d electrons on atomically dispersed cobalt centres in coordination polymers regulate both oxygen reduction reaction (ORR) activity and selectivity for use in zinc–air batteries, *Angew. Chem. Int. Ed. Engl.* 59 (2020) 286–294, <https://doi.org/10.1002/anie.201910879>.
- [109] M.M. Roessler, E. Salvadori, Principles and applications of EPR spectroscopy in the chemical sciences, *Chem. Soc. Rev.* 47 (2018) 2534–2553, <https://doi.org/10.1039/C6CS00565A>.
- [110] J. Zhang, Z. Zhao, Z. Xia, L. Dai, A metal-free bifunctional electrocatalyst for oxygen reduction and oxygen evolution reactions, *Nat. Nanotechnol.* 10 (2015) 444–452, <https://doi.org/10.1038/nnano.2015.48>.
- [111] M. Moloudi, A. Noori, M.S. Rahmanifar, Y. Shabangoli, M.F. El-Kady, N. B. Mohamed, R.B. Kaner, M.F. Mousavi, Layered double hydroxide templated synthesis of amorphous nicofeb as a multifunctional electrocatalyst for overall water splitting and rechargeable Zinc–Air Batteries, *Adv. Energy Mater.* 13 (2023) 2203002, <https://doi.org/10.1002/aenm.202203002>.
- [112] Y. Li, H. Dai, Recent advances in zinc–air batteries, *Chem. Soc. Rev.* 43 (2014) 5257–5275, <https://doi.org/10.1039/C4CS00015C>.
- [113] C. Wang, J. Li, Z. Zhou, Y. Pan, Z. Yu, Z. Pei, S. Zhao, L. Wei, Y. Chen, Rechargeable zinc-air batteries with neutral electrolytes: recent advances, challenges, and prospects, *EnergyChem* 3 (2021) 100055, <https://doi.org/10.1016/j.enchem.2021.100055>.